Title: Facile Mechanochemical Cycloreversion of Polymer Cross-linkers Enhances Tear Resistance

One-Sentence Summary: Replacing conventional covalent crosslinkers with crosslinkers that break more easily in response to force through a cycloreversion reaction improves the ultimate strength and tear resistance of polymer networks.

Authors: Shu Wang[1,2], Yixin Hu[1,2], Tatiana B. Kouznetsova[1,2], Liel Sapir[1,3], Danyang Chen[1,3], Abraham Herzog-Arbeitman[1,4], Jeremiah A. Johnson[1,4]*, Michael Rubinstein[1,2,3,5,6]*, Stephen L. Craig[1,2]*

Affiliations:

[1]NSF Center for the Chemistry of Molecularly Optimized Networks, Duke University; Durham, NC, United States.

[2]Department of Chemistry, Duke University; Durham, NC 27708, United States

[3]Thomas Lord Department of Mechanical Engineering and Materials Science, Duke University; Durham, NC, United States

[4]Department of Chemistry, Massachusetts Institute of Technology (MIT); Boston, MA, United States

[5]Department of Biomedical Engineering, and Physics, Duke University; Durham, NC, United States

[6]Institute for Chemical Reaction Design and Discovery (WPI-ICReDD); Hokkaido University, Sapporo 001-0021, Japan

*Corresponding author. Email: jaj2109@mit.edu (J.A.J.); michael.rubinstein@duke.edu (M.R.); stephen.craig@duke.edu (S.L.C.)

Abstract: Covalent polymer networks are the molecular scaffolds that form the basis of materials in a wide range of both common and highly specialized applications, including tires, rubber bands, contact lenses, and tissue engineering. A covalent polymer network is a single molecule whose fracture and catastrophic failure under load involve the mechanochemical scission of covalent bonds. It is reasonable to expect, therefore, that when all other aspects of network structure and dynamics are effectively unchanged, networks held together with molecular components that break more easily will result in weaker materials. Here, we report that the introduction of scissile cyclobutane-based mechanophore cross-linkers that react via a facile force-triggered cycloreversion leads to network materials that are stronger and tougher than conventionally cross-linked analogs. The cyclobutane mechanophore requires forces of only ~700 pN to break on the timescale of ms, in comparison to ~4 nN for common hydrocarbon controls. Elastomers made from the mechanophore crosslinkers exhibit tearing energies that are up to 9 times greater than that of otherwise indistinguishable elastomers made from the non-mechanophore control crosslinkers. The enhanced toughness from mechanochemically reactive cross-linkers is observed in two different acrylate matrices, in fatigue as well as constant displacement rate tension, and in a gel as well as elastomers. Structure-activity studies reveal that the magnitude of the mechanophore effect depends on molecular details at both the level of the covalent network (the contour length of the primary chain) and the substituents on the cyclobutane, suggesting a pathway for the optimization of polymer properties through the merger of synthetic polymer and small molecule chemistry.

Main Text: The lifetime and utility of covalent rubbery polymer networks are determined by their ability to accommodate large deformation without catastrophic failure. At sufficiently high strains, the network breaks by forming a crack that subsequently propagates through the material to the point of failure. Tearing at the macroscopic level is resisted at the molecular level by polymer chains within the network that need to break in order for the crack to propagate. The scission of covalent chains occurs through a chemical reaction – typically homolytic bond scission that is accelerated by the mechanical tension in overstretched chains at the propagating crack front. It is possible, however, to design and incorporate a small fraction of mechanically scissile functional groups (mechanophores) whose reactivity dominates the chain scission events. In such systems, the mechanical properties of the network might be expected to reflect the force-coupled reactivity of the mechanophores. To that end, a recent study shows that when mechanophores are embedded into the middle of each elastically active network strand (Fig. 1A), the molecular and material properties are correlated in an intuitively satisfying manner: mechanochemical reactions that require less force to break on a given timescale result in weaker polymer networks (*1,2*). We were curious to see if this relationship persists when the mechanophore holds the network together through side-chain cross-linking in randomly cross-linked networks (Fig. 1B). As described below, we find that the material properties again depend dramatically on the force-coupled reactivity of the mechanophore. To our surprise, however, the relationship is reversed from that observed in the end-linked system: crosslinkers that are engineered to react via a more facile mechanically coupled cycloreversion enhance network tearing energy by up to a factor of 9 relative to conventional cross-linker controls.

Our approach is shown in Fig. 1C. Side-chain crosslinked networks with long hydrocarbon polyacrylate backbones (primary chain, light grey chains in Fig. 1, B and C) are formed through reversible addition−fragmentation chain-transfer (RAFT) polymerization of 2-methoxyethyl

acrylate monomer (M). The polymerization is initiated by the photoinitiator (PI), and the average degree of polymerization of the primary chains is controlled by the chain transfer agent (CTA). Polymerizing a pre-gel solution without crosslinker (C) yields linear primary chains as a melt with no significant mechanical integrity while polymerizing it with bis-acrylate crosslinkers **C1** and **C2** separately forms two percolated elastomer networks **E1** and **E2** because the primary chains in **E1** and **E2** are held together by crosslinkers **C1** and **C2**. Crosslinker **C1** is a cis-diaryl substituted cyclobutane-based mechanophore which reacts under tension by means of a force-coupled [2+2] cycloreversion to form two cinnamates (Fig. 1D) (*3*), while crosslinker **C2** consists of common hydrocarbon and carbon-oxygen bonds which are mechanochemically strong (*4,5*). The force-coupled kinetics of **C1** cycloreversion have been characterized by single-molecule force spectroscopy (SMFS) (Fig. S1). The lifetime-force relationship of **C1** and common C-C bond (simulation data by Beyer (*5*)) are shown in Fig. 1E. The force required to achieve lifetimes relevant to material tearing (between microseconds and seconds) is roughly a factor of 5 lower for **C1** than is expected for **C2** and the other molecular components of the networks.

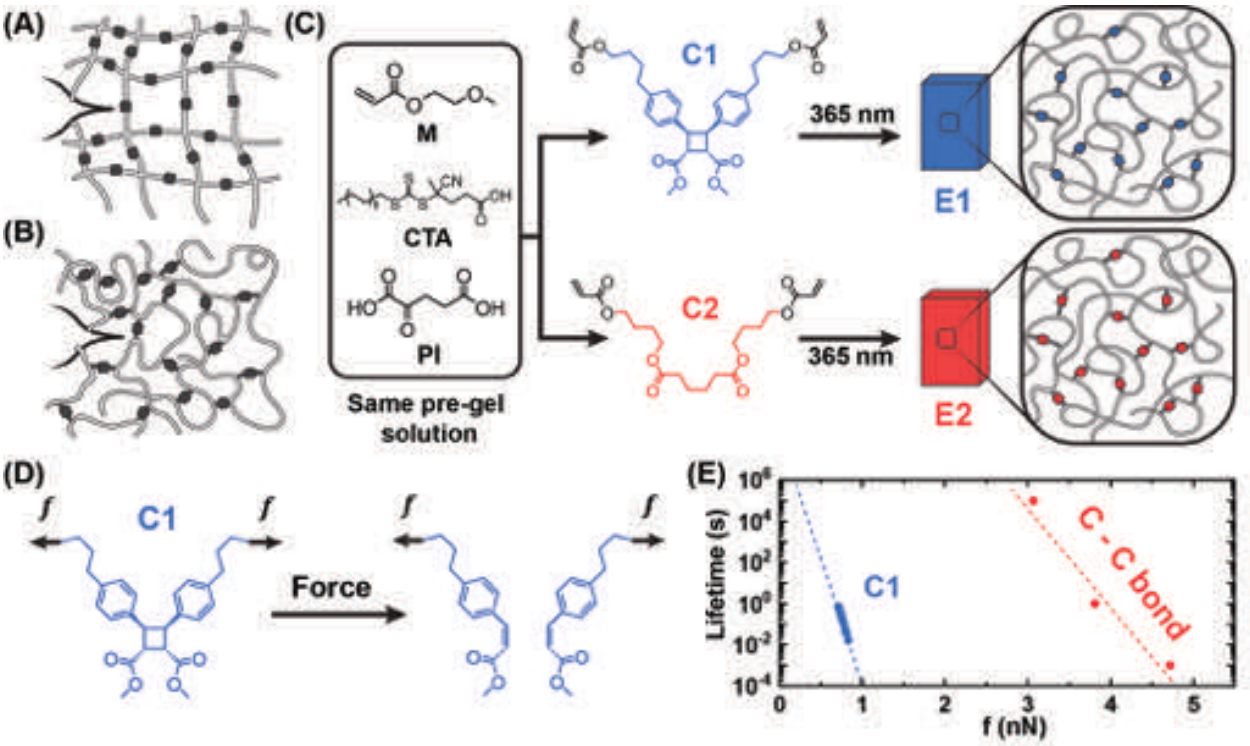

Fig. 1. Networks design and the mechanochemical reactivities of crosslinkers. Mechanophores embedded (**A**) into the middle of chains, and (**B**) as the side-chain crosslinkers of primary chains. (**C**) General procedure for RAFT network preparation. (**D**) Force-triggered cycloreversion of **C1**. (**E**) Lifetime as a function of breaking force for **C1** and common C-C bond. Dash lines are shown as guides.

We start with a stoichiometry of [M] : [C] : [CTA] : [PI] = 1 : 1/50 : 1/1200 : 1/2000. The reactivity of alkyl acrylates is known to be largely independent of the character of the alkyl group (*6*), and so polymerizing the same pre-gel solution with **C1** and **C2** is expected to lead to effectively identical networks that differ only in the mechanically coupled reactivity of the cross-linker. This expectation was verified through several characterizations: (1) Shear moduli of **E1** and **E2** (blue and red in Fig. 2A, respectively) were characterized by small-amplitude oscillatory rheology, and both exhibit similar storage moduli *G'* and loss moduli *G"* across frequencies of 0.1 – 100 Hz. Their storage moduli *G'* are independent of frequency from 0.1 – 10 Hz and are

well above *G"*, indicating **E1** and **E2** are well-formed elastic networks. The average *G'* of **E1** and **E2** at 0.1 Hz are statistically the same ($p = 0.83$): 336 ± 35 and 330 ± 14 kPa, respectively, and well above the modulus due to entanglement $G_e \approx 111 \pm 6$ kPa (Fig. S3). (2) Young's moduli obtained from uniaxial stress-strain curves (Fig. 2B) are indistinguishable; (3) similar sol fractions (Fig. S4A), and (4) similar equilibrium swelling ratios (Fig. S4B). These data suggest that **E1** and **E2** are statistically identical in terms of network connectivity. Furthermore, the glass transition temperatures T_g of **E1** and **E2** are similar and well below room temperature (~ -30 °C) (Fig. S5).

Although these two elastomers have similar network connectivity, we noticed that their unnotched films break very differently when stretched either by hand (not shown) or by DMA (Fig. 2B). Surprisingly, the network **E1** made with weaker crosslinkers is noticeably more difficult to tear than **E2** made with stronger crosslinkers. To quantitatively confirm their difference, the tearing energies Γ of **E1** and **E2** were characterized using the Rivlin-Thomas method on notched films in a pure shear geometry (*7*). The stress-strain curves across five notched samples for each elastomer in Fig. 2C show that **E1** and **E2** have very different critical strains for crack propagation and Γ of **E1** (113.0 ± 9.7 J · m^{-2}) is roughly an order of magnitude higher than Γ of **E2** (11.5 ± 3.7 J · m^{-2}) (Fig. 2D). The impact of cyclobutane reactivity on toughness is almost the direct opposite of that observed in an end-linked system (Fig. 1A), where embedding similar mechanophores into the middle of chains leads to 8-fold lower tearing energy compared to the non-mechanophore control (Fig. 2, E and F) (*1*). Here, stitching polymer chains together through the much mechanically weaker reactant leads to a much stronger material.

The enhanced toughness brought about by replacing **C2** with **C1** is not limited to networks made from a 2-methoxyethyl acrylate co-monomer, to the elastomer state, or to the specific characterization test – although the magnitude of the effect does change. For example, the same

trend observed in tearing is also observed in fatigue testing, which minimizes contributions to the tearing resistance from the energy that is dissipated rather than stored elastically during network stretching (hysteresis) by slowing down the crack growth rate with cyclic loading (*8,9*). As shown in Fig. 2G-H, both **E1** and **E2** have fatigue thresholds below their tearing energies (shaded areas), which is common for elastomers (*8,10*). However, the fatigue threshold of **E1** (52.0 J·m^{-2}) is still much larger than that of **E2** (8.0 J·m^{-2}). Moreover, a similar toughening effect also exists when the 2-methoxyethyl acrylate networks are prepared as organogels (Γ = 62.3 ± 6.4 vs. 18.5 ± 2.3 J · m^{-2}, Fig. S8) and when elastomers are made from ethyl acrylate monomers (Γ = 540 ± 84 vs. 172 ± 25 J · m^{-2}, Fig. S9). See supplementary materials for details.

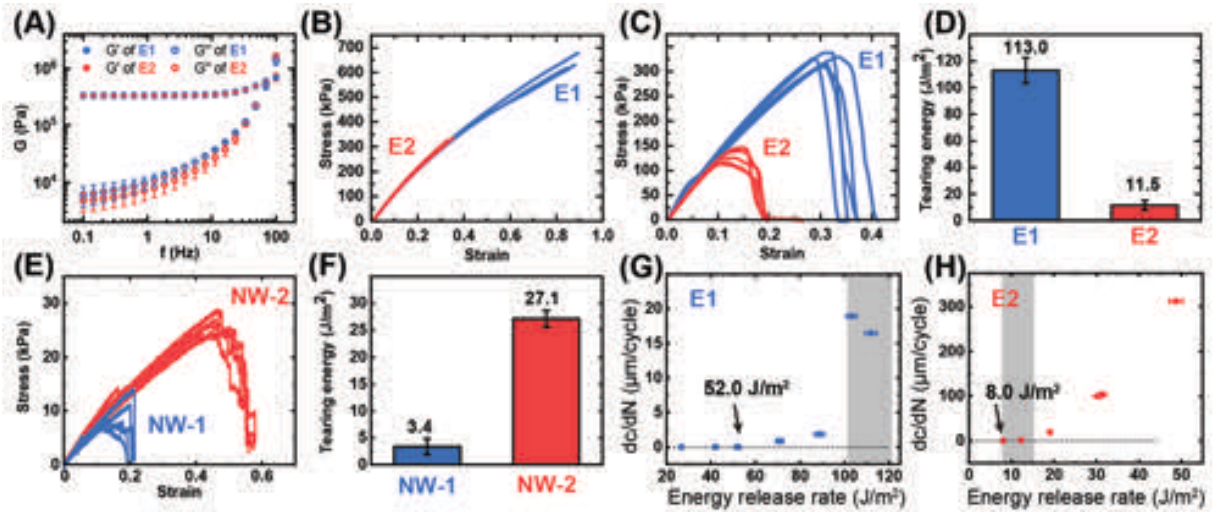

Fig. 2. Mechanical characterizations for elastomers. (**A**) Frequency sweeps (×3 samples each) (strain = 0.5%), uniaxial extension stress-strain curves of (**B**) unnotched (×3 samples each) and (**C**) notched (×5 samples each) samples in pure shear geometry, and (**D**) tearing energies for **E1** and **E2**; $p = 6.5 \times 10^{-6}$. (**E**) Uniaxial tensile test of notched samples in pure shear geometry and (**F**) tearing energies for **NW-1** and **NW-2** adapted from previous work (*1*). Crack growth per

cycle as a function of energy release rate for (**G**) **E1** and (**H**) **E2**. Error bars are standard deviations.

The results raise the important question of why the effect of introducing the same scission reaction in side-chain crosslinked networks is almost the exact opposite of what is observed in the end-linked networks of Fig. 1A. This toughening effect is not due to simple energy dissipation in the bulk, as both *G'* and *G"* are unchanged by the crosslinkers. We hypothesized that the different response to the embedded reactivity originates from an important topological difference. In the end-linked networks of Fig. 1A (*1*), every load-bearing chain has a mechanophore, so increasing the reactivity of the mechanophore increases every scission probability to the same extent. Incorporating the mechanophore as the side-chain crosslinker, however, only weakens the crosslinker and not the primary chain.

The consequences of this topology are proposed in Fig. 3A. Preferential scission through the cycloreversion of intra/intermolecular **C1**, rather than primary chain scission, lengthens rather than removes the bridging chain at the crack interface, which gives rise to the increase in tearing energy. There is no such preferential crosslinker reactivity in **E2**, because the crosslinkers are similarly strong as the primary chain (Fig. 3B). A molecular dynamics simulation of network fracture under uniaxial stretching provides a consistent picture: (1) at high strain, mechanochemically weak crosslinkers in **E1** break almost exclusively while leaving most of the primary chain bonds intact (Fig. S16); and, (2) relevant elastically active strands between crosslinkers, on average, become much longer per bond scission event in **E1** compared to that in **E2** (Fig. S18). Random network cross-linking comprises a complex mixture of intramolecular and intermolecular junctions and loops (*11*). The programmed cycloreversion of intramolecular **C1** releases hidden length in a manner that is reminiscent of noncovalent domain unfolding (*12,13*) and covalent reactive strand extension (*14*), while that of intermolecular **C1** deviates the

crack and increases pathway tortuosity. Based on this picture, the contour length of the primary chain would influence this toughening effect, and so we used the synthetic control afforded by RAFT to vary the degree of polymerization of the primary chains (N_p) (Table S2, see method for calculating N_p in the supplementary materials) while keeping the extent of cross-linking constant.

Elastomers of differing N_p were prepared with either **C1** or **C2**, and the moduli and swelling are again indistinguishable between mechanophore and control networks for all N_p (Fig. 3C, S4). The moduli increase modestly with N_p, as expected due to the decrease in elastically inactive dangling chain ends (*15*). The tearing energies of **E2** do not change much with N_p (Fig. 3D), as is typical of conventionally cross-linked elastomers, whose tearing energy is dominated by the length of the chain between crosslinks (*10*), which is kept almost constant here. The tearing energies of **E1**, however, depend substantially on the contour length of the primary chain (Fig. 3D). When the primary chains are short ($N_p \approx 350$), elastomer **E1** is only slightly stronger than **E2**, but as the primary chains lengthen, the tearing energies of **E1** increase more than 4-fold for $N_p \approx 2000$. The unusual dependence of Γ on N_p in **E1** is consistent with our model; the longer primary chains require a more tortuous path.

The reactivity-enabled toughening afforded by **C1** provides a mechanism to mitigate an otherwise intrinsic tradeoff in polymer network optimization, namely the inverse correlation of modulus and toughness. At fixed $N_p \approx 1400$, increasing the cross-linker content ([C]:[M] = 1:200, 1:100, 1:50) leads to high modulus materials. As expected, this increase in modulus is accompanied by a significant drop of Γ in the control elastomer **E2**, with a scaling exponent of -1.7 that is similar to that reported in other side-chain crosslinked systems (Fig. 3F) (*16,17*). The loss of toughness is attributed to the decreased chain length between cross-linkers (*10*). By comparison, the reactivity engineered into **E1** enables the elastomer to acquire higher stiffness without sacrificing the same extent of tear resistance (scaling exponent of -0.7), because the loss

in toughness due to higher cross-link density is offset by the enhanced toughness afforded by additional mechanophores.

The decrease of Γ for **E1** (Fig. 3F) suggests that the primary chains cannot be completely pulled out before they break, because if tearing energy is dominated by complete chain pull-out (breaking all the **C1** at least along one direction), the tearing energy would increase while the modulus increases, as there are more crosslinkers to break to dissipate energy. This incomplete primary chain pull-out might originate from the entanglement lockup under high tension (*18*). The locked entanglements act like strong crosslinker **C2**, which force the primary chain to break instead of being pulled out. The length scale between two locked entanglements seems to be crosslinking density dependent.

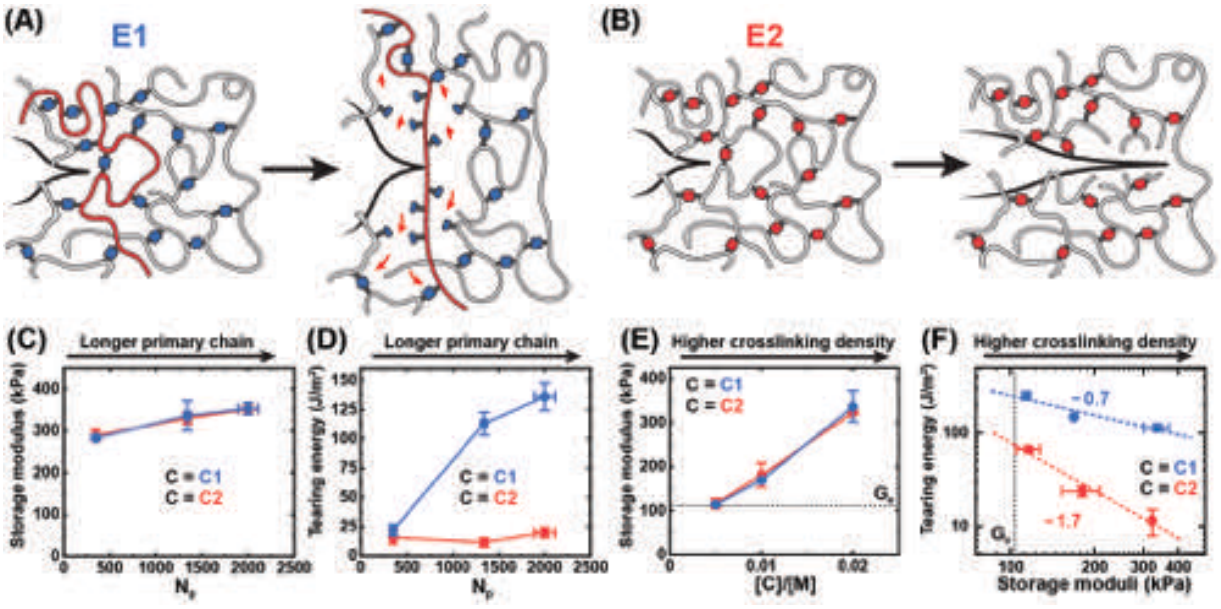

Fig. 3. Toughening mechanism of mechanochemically weak crosslinkers. (**A**) Mechanochemically weak crosslinkers break preferentially before mechanically strong primary chains break in **E1**, which increases the tortuosity of the crack path. (**B**) Crosslinkers that are similarly strong as the primary chains in **E2** do not break preferentially. Cartoons are schematic

only. (**C**) Storage moduli and (**D**) tearing energies of **E1** and **E2** with different N_p. (**E**) Storage moduli of **E1** and **E2** with different crosslinking densities. (**F**) Log-log plot of Γ vs. G' of **E1** and **E2** with different crosslinking densities. Dashed lines are power-law fittings. Error bars are standard deviations.

Finally, we wondered how the reactivity of the cross-linker relative to the primary chain influences the effect. We synthesized another mechanophore crosslinker **C3** of intermediate strength (Fig. S10; relevant force at break is roughly half that of conventional polymer components and just over twice that of **C1**). Interestingly, **E3** results in only a very modest toughening effect (factor of <2 vs. >9 for otherwise identical networks; see Fig. S10), which is likely because the larger mechanochemical strength of **C3** compared to **C1** suppresses the lengthening efficiency of bridging chains before primary chains break. This result suggests that further decrease in the mechanochemical strength of the crosslinker while other components remain unchanged might potentially lead to tougher networks, yet such a crosslinker could suffer from poor thermal stability, which risks the physical integrity of the networks. The extreme case is the crosslinker has no strength (i.e., no crosslinker) or very low crosslinking density. Although, depending on the loading rate, such highly entangled systems could achieve high tearing energy through non-specific near crack dissipation, their stiffness is no longer tunable with crosslinkers (*16,17*).

The work reported here has implications for the use of "weak" bonds to toughen covalent polymer networks. Typically, toughening a network through weak cross-linkers involves the use of dynamic interactions, such as ionic bonding (*19*), hydrogen bonding (*20*), or the reversible formation of stable radicals (*21,22*), all of which lead to a fluid network structure on longer timescales or at higher temperatures and have the capacity to recombine during or following scission. No such scrambling or reformation is accessible here, demonstrating that preferential

bond scission at the propagating crack front alone is sufficient to provide a substantive toughening effect. We note that pathway tortuosity at the macroscale, for example in composites, is an established toughening mechanism (*23*), and the results observed here indicate that molecular analogues of that behavior likely contribute to the more complex toughening mechanisms at play in reversible networks. For both those dynamic networks and the static covalent networks demonstrated here, the primary chain length effect offers a clear design principle for optimizing reactivity-enabled toughening without losing stiffness. An advantage of toughening through the programmed reactivity of covalent cross-linkers is that the properties of the mechanophore network are indistinguishable from those of the conventional network, with the exception of the preferential scission behavior that occurs only when and where necessary to inhibit material tearing and fatigue; even the primary chain effect has a very modest impact on low-strain mechanical properties relative to the impact on toughness. The utility of **C1** shows that these gains can be realized with mechanophores of good thermal stability (*3*) (Fig. S14), offering the opportunity to further optimize toughness through the judicious design of the scissile reaction mechanism. Going forward, the synthetic control available at both the level of the mechanophore cross-linker and the constituent polymer chain offers a platform for the quantitative understanding of how mechanochemically weak structures influence the mechanical properties of polymer networks.

References and Notes

1. Wang, S., Beech, H. K., Bowser, B. H., Kouznetsova, T. B., Olsen, B. D., Rubinstein, M. & Craig, S. L. Mechanism Dictates Mechanics: A Molecular Substituent Effect in the Macroscopic Fracture of a Covalent Polymer Network. *J. Am. Chem. Soc.* **143**, 3714–3718

(2021).

2. Bowser, B. H., Wang, S., Kouznetsova, T. B., Beech, H. K., Olsen, B. D., Rubinstein, M. & Craig, S. L. Single-Event Spectroscopy and Unravelling Kinetics of Covalent Domains Based on Cyclobutane Mechanophores. *J. Am. Chem. Soc.* **143**, 5269–5276 (2021).

3. Zhang, H., Li, X., Lin, Y., Gao, F., Tang, Z., Su, P., Zhang, W., Xu, Y., Weng, W. & Boulatov, R. Multi-modal mechanophores based on cinnamate dimers. *Nat. Commun.* **8**, 1147 (2017).

4. Grandbois, M., Beyer, M., Rief, M., Clausen-Schaumann, H. & Gaub, H. E. How strong is a covalent bond. *Science* **283**, 1727–1730 (1999).

5. Beyer, M. K. The Mechanical Strength of a Covalent Bond Calculated by Density Functional Theory. *J. Chem. Phys.* **112**, 7307–7312 (2000).

6. Haehnel, A. P., Schneider-Baumann, M., Arens, L., Misske, A. M., Fleischhaker, F. & Barner-Kowollik, C. Global trends for k_p? the influence of ester side chain topography in alkyl (Meth)Acrylates - Completing the data base. *Macromolecules* **47**, 3483–3496 (2014).

7. Rivlin, R. S. & Thomas, A. G. Rupture of rubber. I. Characteristic energy for tearing. *J. Polym. Sci.* **10**, 291–318 (1953).

8. Lake, G. J. & Lindley, P. B. The mechanical fatigue limit for rubber. *J. Appl. Polym. Sci.* **9**, 1233–1251 (1965).

9. Tang, J., Li, J., Vlassak, J. J. & Suo, Z. Fatigue fracture of hydrogels. *Extrem. Mech. Lett.* **10**, 24–31 (2017).

10. Lake, G. J. & Thomas, A. G. The Strength of Highly Elastic Materials. *Proc. R. Soc.*

London, Ser. A Math. Phys. Sci. **300**, 108–119 (1967).

11. Wang, J., Wang, R., Gu, Y., Sourakov, A., Olsen, B. D. & Johnson, J. A. Counting loops in sidechain-crosslinked polymers from elastic solids to single-chain nanoparticles. *Chem. Sci.* **10**, 5332–5337 (2019).

12. Guan, Z., Roland, J. T., Bai, J. Z., Ma, S. X., McIntire, T. M. & Nguyen, M. Modular Domain Structure: A Biomimetic Strategy for Advanced Polymeric Materials. *J. Am. Chem. Soc.* **126**, 2058–2065 (2004).

13. Fang, J., Mehlich, A., Koga, N., Huang, J., Koga, R., Gao, X., Hu, C., Jin, C., Rief, M., Kast, J., Baker, D. & Li, H. Forced protein unfolding leads to highly elastic and tough protein hydrogels. *Nat. Commun.* **4**, (2013).

14. Wang, Z., Zheng, X., Ouchi, T., Kouznetsova, T. B., Beech, H. K., Av-Ron, S., Matsuda, T., Bowser, B. H., Wang, S., Johnson, J. A., Kalow, J. A., Olsen, B. D., Gong, J. P., Rubinstein, M. & Craig, S. L. Toughening hydrogels through force-triggered chemical reactions that lengthen polymer strands. *Science* **374**, 193 (2021).

15. Henkel, R., Vana, P., Henkel, R. & Vana, P. The Influence of RAFT on the Microstructure and the Mechanical Properties of Photopolymerized Poly(butyl acrylate) Networks. *Macromol. Chem. Phys.* **215**, 182–189 (2014).

16. Kim, J., Zhang, G., Shi, M. & Suo, Z. Fracture, fatigue, and friction of polymers in which entanglements greatly outnumber cross-links. *Science* **374**, 212–216 (2021).

17. Zheng, D., Lin, S., Ni, J. & Zhao, X. Fracture and fatigue of entangled and unentangled polymer networks. *Extrem. Mech. Lett.* **51**, 101608 (2022).

18. Zheng, Y., Tsige, M. & Wang, S. Q. Molecular Dynamics Simulation of Entangled Melts

at High Rates: Identifying Entanglement Lockup Mechanism Leading to True Strain Hardening. *Macromol. Rapid Commun.* 2200159 (2022).

19. Sun, J. Y., Zhao, X., Illeperuma, W. R., Chaudhuri, O., Oh, K. H., Mooney, D. J., Vlassak, J. J. & Suo, Z. Highly stretchable and tough hydrogels. *Nature* **489**, 133–136 (2012).

20. Neal, J. A., Mozhdehi, D. & Guan, Z. Enhancing Mechanical Performance of a Covalent Self-Healing Material by Sacrificial Noncovalent Bonds. *J. Am. Chem. Soc.* **137**, 4846–4850 (2015).

21. Sakai, H., Aoki, D., Seshimo, K., Mayumi, K., Nishitsuji, S., Kurose, T., Ito, H. & Otsuka, H. Visualization and Quantitative Evaluation of Toughening Polymer Networks by a Sacrificial Dynamic Cross-Linker with Mechanochromic Properties. *ACS Macro Lett.* **9**, 1108–1113 (2020).

22. Watabe, T., Aoki, D. & Otsuka, H. Polymer-Network Toughening and Highly Sensitive Mechanochromism via a Dynamic Covalent Mechanophore and a Multinetwork Strategy. *Macromolecules* **55**, 5795–5802 (2022).

23. Ritchie, R. O. Mechanisms of fatigue-crack propagation in ductile and brittle solids. *Int. J. Fract.* **100**, 55–83 (1999).

Acknowledgments: We thank B. D. Olsen for helpful discussion, and K.A. Gall lab for access to the fatigue test instrument.

Funding: This work was supported by the NSF Center for the Chemistry of Molecularly Optimized Networks (MONET), CHE-2116298, to J.A.J., M.R., and S.L.C.

Author contributions:

Conceptualization: SW, AH, JAJ, MR, SLC

Methodology: SW, YH, TBK, LS, DC, AH, JAJ, MR, SLC

Investigation: SW, YH, TBK, LS, DC

Funding acquisition: JAJ, MR, SLC

Project administration: JAJ, MR, SLC

Supervision: JAJ, MR, SLC

Writing – original draft: SW, SLC

Writing – review & editing: SW, YH, TBK, LS, DC, AH, JAJ, MR, SLC

Competing interests: S.W. is also affiliated with the Department of Mechanical Engineering, Massachusetts Institutes of Technology (MIT), 77 Massachusetts Ave., Boston, MA 02139, United States.

Data and materials availability: All data are available in the main text or the supplementary materials.

Supplementary Materials

Materials and Methods

Supplementary Text

Figs. S1 to S15

Tables S1 to S2

References (*24–32*)

Movie S1

Science
AAAS

Supplementary Materials for

Facile Mechanochemical Cycloreversion of Polymer Cross-linkers Enhances Tear Resistance

Shu Wang[1,2], Yixin Hu[1,2], Tatiana B. Kouznetsova[1,2], Liel Sapir[1,3], Danyang Chen[1,3], Abraham Herzog-Arbeitman[1,4], Jeremiah A. Johnson[1,4]*, Michael Rubinstein[1,2,3,5,6]*, Stephen L. Craig[1,2]*

Correspondence to: jaj2109@mit.edu (J.A.J.); michael.rubinstein@duke.edu (M.R.); stephen.craig@duke.edu (S.L.C.)

This PDF file includes:

Materials and Methods
Supplementary Text
Figs. S1 to S20
Tables S1 to S2
Caption for Movie S1

Other Supplementary Materials for this manuscript include the following:

Movies S1

Materials and Methods

Materials

Lab general solvents (dichloromethane, acetonitrile, hexane, ethyl acetate, acetone, tetrahydrofuran, dioxane, methanol, dimethyl formaldehyde) were purchased from VWR or Sigma Aldrich. Hydrogen was purchased from Airgas. 4-bromo-cinnamic acid, 4-(dimethylamino)pyridine (DMAP), 3-(3-dimethylaminopropyl)-1-ethyl-carbodiimide hydrochloride (EDC·HCl), copper (I) iodide (CuI), Sodium iodide (NaI), trans-N,N-dimethylcyclohexane-1,2-diamine, 3-Butyn-1-ol, bis(triphenylphosphine)palladium(II) dichloride, diisopropylamine, palladium on carbon (10 wt%), acrylic acid, 4-hydroxybutyl acrylate, adipic acid, 2-hydroxyethyl acrylate, pyridinium p-toluenesulfonate (PPTS), 2-methoxypropene, triethylamine (TEA), Grubbs II catalyst, 4-pentenoic anhydride, 9-oxabicyclo[6.1.0]non-4-ene, ethyl acrylate, 2-methoxylethyl acrylate, 4-Cyano-4-[(dodecylsulfanylthiocarbonyl)sulfanyl]pentanoic acid, α-ketoglutaric acid, and propylene carbonate were purchased from Sigma Aldrich, or Alfa Aesar, or ChemImpex, or Ambeed Inc., and used without further purification. Borosilicate glass plates, low friction transparent FEP tape (0.0035" thick), low friction PTFE tape (0.012" thick) are purchased from McMASTER-CARR.

General methods

^{1}H NMR and ^{13}C NMR spectra were collected on a 500 MHz Bruker spectrometer. ^{1}H shifts are reported as chemical shift, multiplicity, coupling constant if applicable, and relative integral. Multiplicities are reported as: singlet (s), doublet (d), doublet of doublets (dd), doublet of triplets (dt), doublet of doublet of doublets (ddd), doublet of doublet of triplets (ddt), triplet (t), triplet of doublets (td), quartet (q), multiplet (m), or broad (br). High-resolution mass spectra were collected on an Agilent LCMS-TOF-DART at Duke University's Mass Spectrometry Facility or an JEOL AccuTOF-DART at Massachusetts Institute of Technology's Mass Spectrometry Facility.

Flash chromatography was performed using Silicycle SiliaFlash® F60 gel (40-63 μm particle size, 230-400 mesh) and medium pressure liquid chromatography (MPLC) was performed on a Teledyne ISCO CombiFlash Rf 200.

Gel permeation chromatography (GPC) was performed on in-line two columns (Agilent PLgel 105 Å, 7.5 x 300 mm, 5μm, part number PL1110-6550) at room temperature using inhibitor free THF at a flow rate of 1.0 mL/min. The flow rate was set using an Agilent 1260 Infinity Isocratic pump, molecular weights were calculated using in line Wyatt Optilab T-rEX refractive index detector and Wyatt miniDAWN TREOS multiangle light scattering detector, and UV absorbance was measured with an in-line Agilent 1260 Infinity UV detector. The UV detector monitored 190 to 800 nm with step of 2.0 nm and slit width of 4.0 nm. The refractive index increment (dn/dc) values were determined by using on-line 100% mass recovery assumption calculations built into Wyatt Astra software using injections of known concentration and mass. Before GPC analysis, 1-2 mg/mL in THF solutions were filtered through a 0.2 μm pore size PTFE syringe filters.

The AFM pulling experiments were conducted in toluene at an ambient temperature (~23˚C) in the same manner as described previously (*24 – 28*) using a homemade AFM, which was constructed using a Bruker (previously Digital Instruments) Multimode AFM head mounted on top of a piezoelectric positioner (Physik Instrumente, GmbH), similar to the one described in detail previously (*29*). Sharp Microlever silicon probes (MSNL) were purchased from Bruker (Camarillo, CA) and the force curves used for analysis were obtained with rectangular-shaped cantilevers (205 μm x 15 μm, nominal tip radius ~2 nm, nominal spring constant k ~ 0.02 N/m, frequency ~ 15 kHz). Multiple probes of the same type were used throughout the course of the experiments. The spring constant of each cantilever was calibrated in air, using the thermal noise method, based on the energy equipartition theorem as described previously (*30*). Cantilever tips were prepared by soaking in piranha solution for ~15 min at room temperature. Silicon surfaces were prepared by soaking ~30 min in hot piranha solution, followed by washing with DI-water and drying under a stream of nitrogen. The surface and cantilever were then placed in a UVO cleaner (ozone produced through UV light) for 15 min. After ozonolysis, the cantilever was mounted, and ~20 μL of a ~0.1-0.05 mg mL^{-1} polymer solution was added to the silicon surface and allowed to dry. Measurements were carried out in a fluid cell with scanning set for a series of constant velocity approaching/retracting cycles.

Rheological measurements were conducted on an Anton Paar MCR 302 rheometer with a disposable 8 mm parallel plate geometry. Uniaxial tensile tests and tearing energy measurements were performed on a TA Instruments RSA III Dynamic Mechanical Analyzer (force resolution: 0.0001 N, displacement resolution: 1 μm) at Duke University's Shared Material Instrument Facility (SMIF). Fatigue tests were performed on a Test Resources 910LX25 dynamic & fatigue test machine (force resolution: 0.0001 N, displacement resolution: 1 μm).

Supplementary Text

Chemical synthesis

1) Synthesis of **C1**

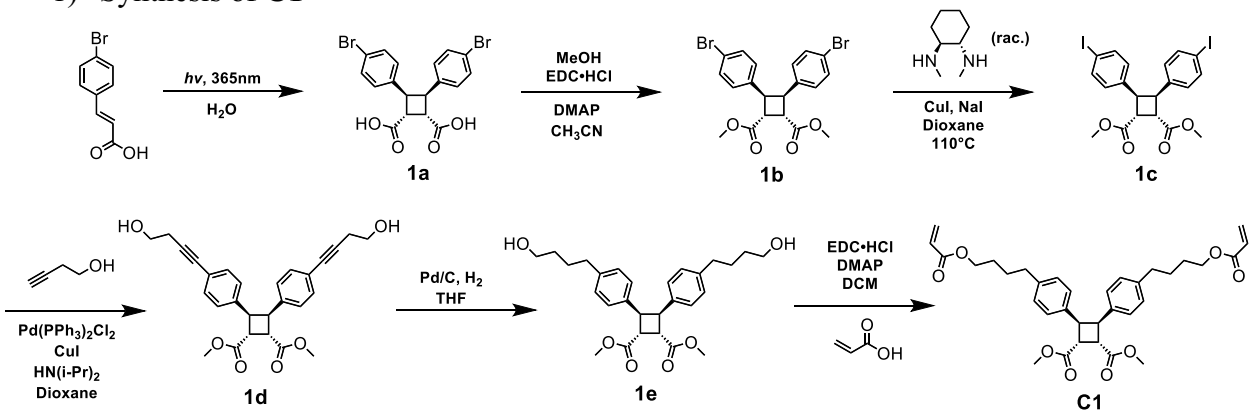

Synthesis of 1b. Compound **1a** was synthesized as previously reported (*1*). To a 250 mL round bottom flask (RBF), compound **1a** (7 g, 15.4 mmol) was mixed with 150 mL acetonitrile. EDC·HCl (8.9 g, 46.4 mmol) was added portion-wise. The solid first dissolved, and then the solution became cloudy again. DMAP (750 mg, 6 mmol) and MeOH (2.5 mL, 62 mmol) were then added to the solution. The reaction was stirred at r.t. for overnight. After the reaction completed, the solution was concentrated using rotary evaporator and diluted with 200 mL ethyl acetate. The solution was washed with DI water (150 mL×2) and brine (150mL×1). EA phase was collected and dried with $MgSO_4$. After filtration, the solution was concentrated onto silica. Column chromatography (SiO_2, 0 ~ 40% EtOAC / hexane gradient eluent) gave compound **1b** as a white solid (6.9 g). ^{1}H NMR (500 MHz, $CDCl_3$): δ 7.27 - 7.26 (d, J = 8.4 Hz, 4H), 6.79 - 6.77 (d, J = 8.4 Hz, 4H), 4.34 - 4.33 (m, 2H), 3.76 - 3.75 (m, 8H). ^{13}C NMR (126 MHz, $CDCl_3$) δ 172.62, 138.21, 133.21, 129.55, 120.77, 54.05, 44.41, 42.79. HRMS-ESI (m/z): $[M + H]^+$ calculated for $C_{20}H_{18}Br_2O_4$, 480.9647; observed 480.9643.

Synthesis of 1c. To a 300 mL pressure vessel charged with a stir bar, compound **1b** (6.9 g, 14.3 mmol) was mixed with 35 mL Dioxane. CuI (273 mg, 1.43 mmol) and NaI (8.63 g, 57.2 mmol) were added. The mixture was purged with N_2 for 10 mins. Trans-N,N-dimethylcyclohexane-1,2-diamine (448.5 μL, 2.86 mmol) was added using micropipette. The vessel was capped with PTFE cap and heated to 110°C. The reaction was stirred for 24h. The vessel was cooled to room temperature, and the mixture was poured onto a short silica plug (ethyl acetate as eluent) to give compound **1c** as thick pale-yellow oil (~ 8.5 g). NMR spectrum showed clean product and the compound was directly used in next step without further purification. ^{1}H NMR (500 MHz, $CDCl_3$): δ 7.47 - 7.46 (d, J = 8.4 Hz, 4H), 6.67 - 6.65 (d, J = 8.3 Hz, 4H), 4.32 - 4.21 (m, 2H), 3.74 - 3.73 (m, 8H). ^{13}C NMR (126 MHz, $CDCl_3$) δ 173.84, 138.08, 137.48, 128.77, 91.38, 52.44, 45.11, 42.43.

Synthesis of 1d. To a 500 mL RBF charged with a stir bar, compound **1c** (~ 8.5 g, ~ 14.3 mmol) was mixed with 150 mL Dioxane. Diisoproypyl amine (12 mL, 85.8 mmol) was added. The mixture was purged with N_2 for 10 mins. Under nitrogen atmosphere, CuI (545 mg, 2.86 mmol, 0.2 equiv. to **1c**) and $Pd(PPh_3)_2Cl_2$ (1 g, 1.43 mmol, 0.1 equiv. to **1c**) were added sequentially. The solution turned dark immediately when $Pd(PPh_3)_2Cl_2$ was added. The reaction

was stirred under N_2 atmosphere for overnight. After the reaction was finished, the solution was filtered with celite. The filtrate was diluted with EA and washed with dilute (1~2 %) HCl DI water solution (150 mL×2) and brine (150mL×1). EA phase was collected and dried over $MgSO_4$. Column chromatography (SiO_2, 0 ~ 80% EtOAC / hexane gradient eluent) gave compound **1d** as thick yellow oil (6.1 g). The yellow color was likely due to the metal residual, which can be removed by QuadraPure® TU. If not pure by NMR, repeat the chromatography. ^{1}H NMR (500 MHz, DMSO): δ 7.11 - 7.09 (d, J = 8.4 Hz, 4H), 7.01- 6.99 (d, J = 8.5 Hz, 4H), 4.86 - 4.84 (t, J = 5.6 Hz, 2H), 4.25 - 4.24 (m, 2H), 4.00 - 3.98 (m, 2H), 3.64 (s, 6H), 3.55 – 3.51 (td, *J* = 6.9, 5.6 Hz, 4H), 2.49 – 2.47 (t, 4H). ^{13}C NMR (126 MHz, DMSO) δ 172.04, 139.85, 129.97, 128.57, 120.37, 88.42, 81.09, 60.66, 52.46, 45.15, 42.36, 23.78. HRMS-ESI (m/z): $[M + H]^+$ calculated for $C_{28}H_{28}O_6$, 461.1959; observed 461.1958.

Synthesis of 1e. To a 500 mL three-neck RBF charged with a stir bar, compound **1d** (6.1 g, 13.2 mmol) was dissolved in 300 mL THF. The solution was purged with N_2 for 10 min. Under nitrogen atmosphere, Pd/C (10% Pd) (2 g) was added portion-wise. Large amount of Pd/C was added because some ligands that carried over from the last step can poison Pd/C. The mixture was purged with N_2 for another 10 min. The hydrogen balloon was connected to the RBF. The mixture was purged with hydrogen for 10 min and was allowed to react under hydrogen atmosphere for 24 h. After the reaction was finished, the solution was filtered with celite. The filtrate was loaded onto silica by rotary-evaporating the solvent. Column chromatography (SiO_2, 0 ~ 80% EtOAC / hexane gradient eluent) gave compound **1e** as thick colorless oil (3.5 g). ^{1}H NMR (500 MHz, $CDCl_3$): δ 6.91 – 6.90 (d, J = 8.2 Hz, 4H), 6.82 - 6.80 (d, J = 8.1Hz, 4H), 4.34 - 4.32 (m, 2H), 3.82 - 3.81 (m, 2H), 3.74 (s, 6H), 3.60 - 3.58 (t, J = 6.4 Hz, 4H), 2.51 - 2.48 (t, J = 7.5 Hz, 4H), 1.60 – 1.45 (m, 12H). ^{13}C NMR (126 MHz, $CDCl_3$) δ 173.76, 143.51, 136.07, 128.14, 127.08, 65.66, 53.54, 46.61, 43.37, 35.83, 33.00, 29.10. HRMS-ESI (m/z): $[M + H]^+$ calculated for $C_{28}H_{36}O_6$, 469.2585; observed 469.2590. $[M + Na]^+$ calculated for $C_{28}H_{36}O_6$ 491.2404; observed 491.2406.

Synthesis of C1. To a 250 mL round bottom flask (RBF), acrylic acid (461 mg, 6.4 mmol), compound **1e** (1 g, 2.13 mmol), DMAP (104.3 mg, 0.85 mmol) were dissolved in 20 mL DCM. EDC·HCl (1.23 g, 6.4 mmol) was added portion-wise at the end. The reaction was stirred at r.t. for overnight. After the reaction completed, the solution was concentrated using rotary evaporator and diluted with 200 mL ethyl acetate. The solution was washed with DI water (150 mL×2) and brine (150mL×1). EA phase was collected and dried with $MgSO_4$. After filtration, the solution was concentrated onto silica. Column chromatography (SiO_2, 0 ~ 40% EtOAC / hexane gradient eluent) gave compound **C1** (0.75 g). *The crosslinker C1 can self-crosslink at high concentration under vacuum, thus it was directly prepared as a stock solution (200 ~ 300 mg/mL) in dioxane.* ^{1}H NMR (500 MHz, $CDCl_3$): δ 6.91 – 6.89 (d, J = 8.1 Hz, 4H), 6.82 - 6.81 (d, J = 8.1Hz, 4H), 6.40 – 6.36 (dd, J = 17.3, 1.5 Hz, 2H), 6.13 – 6.07 (dd, J = 17.3, 10.4 Hz, 2H), 5.82 – 5.80 (dd, J = 10.5, 1.5 Hz, 2H), 4.34 - 4.33 (m, 2H), 4.13 – 4.10 (t, 4H), 3.83 - 3.80 (m, 2H), 3.74 (s, 6H), 2.52 - 2.48 (t, 4H), 1.62 – 1.57 (p, 8H). ^{13}C NMR (126 MHz, $CDCl_3$) δ 172.44, 168.45, 140.09, 136.21, 131.07, 128.69, 128.14, 127.94, 65.19, 52.27, 44.80, 42.96, 35.75, 28.12, 27.64. HRMS-ESI (m/z): $[M + H]^+$ calculated for $C_{34}H_{40}O_8$, 577.2796; observed 577.2798. $[M + Na]^+$ calculated for $C_{34}H_{40}O_8$ 599.2615; observed 599.2612.

2) Synthesis of **C2**

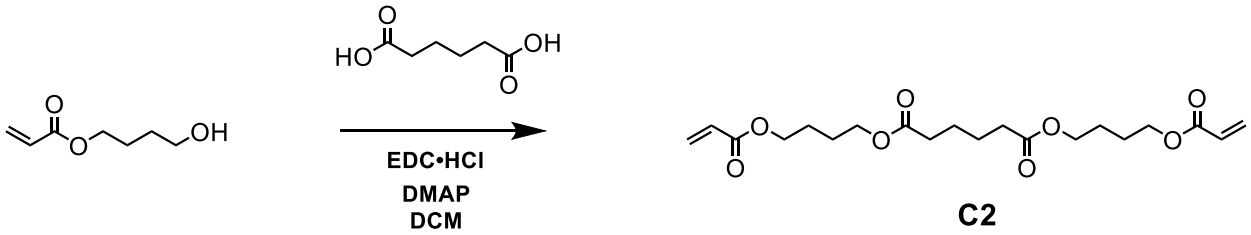

C2

To a 500 mL round bottom flask (RBF), adipic acid (4 g, 27.3 mmol), EDC·HCl (10.5 g, 55 mmol), DMAP (0.67 g, 5.5 mmol) were added sequentially to 200 mL DCM. 4-hydroxybutyl acrylate (10 g, 111 mmol) was added at the end. The reaction was stirred at r.t. for overnight. After the reaction completed, the solution was concentrated using rotary evaporator and diluted with 200 mL ethyl acetate. The solution was washed with DI water (150 mL×2) and brine (150mL×1). EA phase was collected and dried with $MgSO_4$. After filtration, the solution was concentrated onto silica. Column chromatography (SiO_2, 0 ~ 40% EtOAC / hexane gradient eluent) gave compound **C2** (~ 6 g). *The crosslinker **C2** can self-crosslink at high concentration under vacuum, thus it was directly prepared as a stock solution (200 ~ 300 mg/mL) in dioxane.* ^{1}H NMR (500 MHz, $CDCl_3$): δ 6.34 – 6.40 (dd, J = 17.4, 1.4 Hz, 2H), 6.13 – 6.07 (dd, J = 17.3, 10.4 Hz, 2H), 5.83 – 5.80 (dd, J = 10.4, 1.5 Hz, 2H), 4.18 – 4.18 (t, J = 6.0 Hz, 4H), 4.08 – 4.10 (t, J = 6.1 Hz, 4H), 2.33 – 2.30 (m, 4H), 1.76 – 1.63 (m, 12H). ^{13}C NMR (126 MHz, $CDCl_3$) δ 173.41, 166.29, 130.85, 128.55, 64.10, 63.95, 33.96, 25.42, 24.48. HRMS-ESI (m/z): $[M + H]^+$ calculated for $C_{20}H_{30}O_8$, 399.2013; observed 399.2013. $[M + Na]^+$ calculated for $C_{20}H_{30}O_8$ 421.1833; observed 421.1836.

3) Synthesis of **C3**

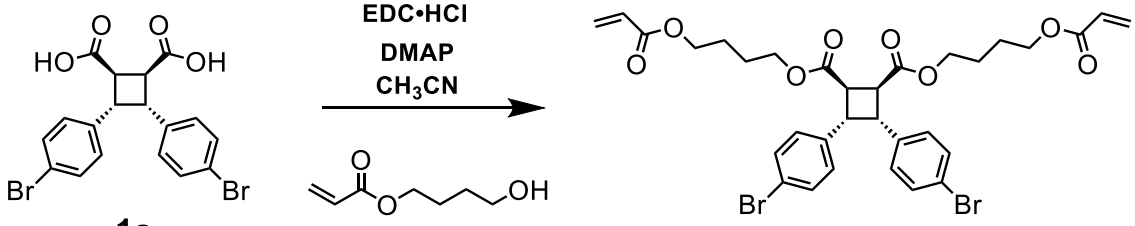

1a **C3**

To a 500 mL round bottom flask (RBF), **1a** (2 g, 4.4 mmol), EDC·HCl (1.69 g, 8.9 mmol), DMAP (108 mg, 0.88 mmol) were added sequentially to 50 mL acetonitrile. 4-hydroxybutyl acrylate (1.4 g, 9.7 mmol) was added at the end. The reaction was stirred at r.t. for overnight. After the reaction completed, the solution was concentrated using rotary evaporator and diluted with 200 mL ethyl acetate. The solution was washed with DI water (150 mL×2) and brine (150mL×1). EA phase was collected and dried with $MgSO_4$. After filtration, the solution was concentrated onto silica. Column chromatography (SiO_2, 0 ~ 40% EtOAC / hexane gradient eluent) gave compound **C3** (~ 2 g). *The crosslinker **C3** can self-crosslink at high concentration under vacuum, thus it was directly prepared as a stock solution (200 ~ 300 mg/mL) in dioxane.* ^{1}H NMR (500 MHz, $CDCl_3$): δ 7.28 – 7.26 (d, J = 8.3 Hz, 4H), 6.81 – 6.79 (d, J = 8.2 Hz, 4H), 6.42 – 6.38 (dd, J = 17.4, 1.4 Hz, 2H), 6.15 – 6.09 (dd, J = 17.3, 10.4 Hz, 2H), 5.84 – 5.82 (dd, J = 10.4, 1.4 Hz, 2H), 4.33 - 4.32 (m, 2H), 4.20 – 4.17 (m, 8H), 3.76 – 3.74 (m, 2H), 1.78 – 1.71 (m, 8H). ^{13}C NMR (126 MHz, $CDCl_3$) δ172.16, 166.26, 137.38, 131.47, 130.93, 129.54, 128.50, 120.74, 64.81, 64.00, 44.50, 43.41, 25.38, 25.36. HRMS-ESI (m/z): $[M + H]^+$ calculated for

$C_{32}H_{34}Br_2O_8$, 705.0693; observed 705.0681. $[M + NH_4]^+$ calculated for $C_{32}H_{34}Br_2O_8$ 722.0959; observed 722.0950. $[M + Na]^+$ calculated for $C_{32}H_{34}Br_2O_8$ 727.0513; observed 727.0539.

4) Synthesis of **C4**

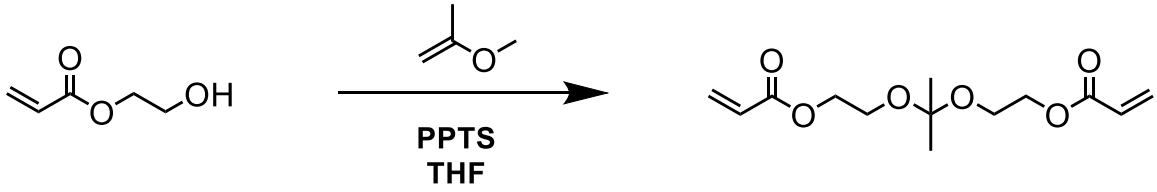

To a 50 mL round bottom flask (RBF) charged with a stir bar, 2-hydroxyethyl acrylate (5 g, 4.95 mL, 43 mmol) and pyridinium p-toluenesulfonate (PPTS) (500 mg, 2 mmol) were added sequentially to 15 mL THF. 2-Methoxypropene (1.67 g, 2.22 mL, 23 mmol) solution in 15 mL THF was added dropwise at 0°C. The reaction was allowed to react for overnight. After reaction was finished, a few drops of triethyl amine (TEA) were added to the solution, and the solution was concentrated onto silica. Column chromatography (SiO_2, 0 ~ 40% EtOAC / hexane gradient eluent, 1% TEA was added) gave compound **C3** (~ 3 g). The crosslinker C3 can self-crosslink at high concentration under vacuum, thus it was directly prepared as a stock solution (~ 200 mg/mL) in DCM. ^{1}H NMR (500 MHz, $CDCl_3$): δ 6.40 – 6.36 (dd, J = 17.3, 1.5 Hz, 2H), 6.13 – 6.08 (dd, *J* = 17.4, 10.4 Hz, 2H), 5.82 – 5.77 (dd, *J* = 10.5, 1.5 Hz, 2H), 4.29 – 4.19 (m, 4H), 3.67 – 3.65 (m, 4H), 1.35(s, 6H). ^{13}C NMR (126 MHz, $CDCl_3$) δ 166.19, 131.03, 128.37, 100.29, 63.93, 58.97, 24.84. HRMS-ESI (m/z): $[M + Na]^+$ calculated for $C_{13}H_{20}O_6$ 295.1152; observed 295.1152.

5) Synthesis of **P1**

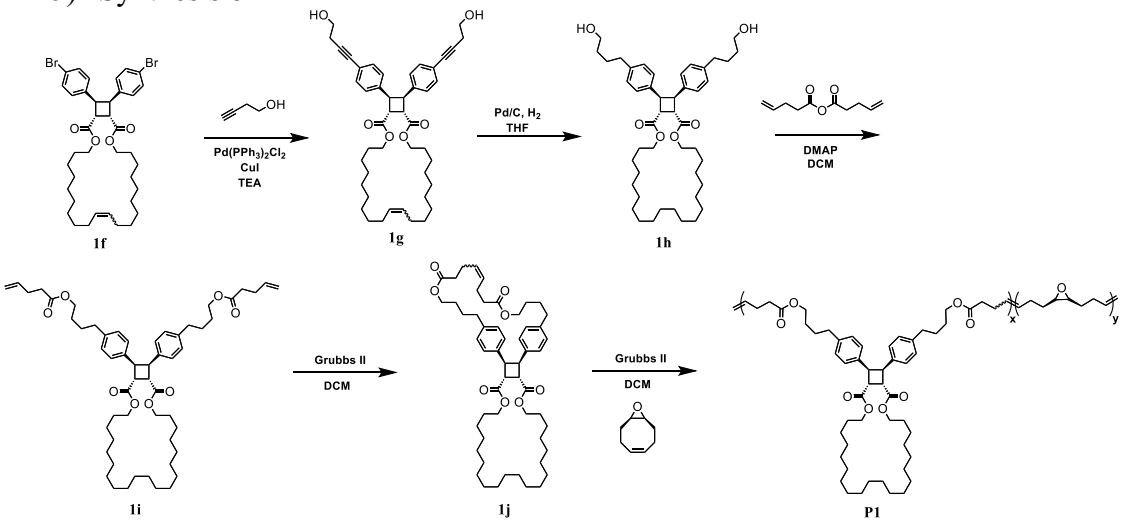

Synthesis of 1g. Compound **1f** was synthesized as previously reported (*2*). To a 25 mL RBF charged with a stir bar, compound **1f** (500 mg, 0.68 mmol) and 3-Butyn-1ol (124 µL, 115 mg, 1.6 mmol) were mixed with 8.2 mL triethyl amine (TEA). The mixture was purged with N_2 for 10 mins. Under nitrogen atmosphere, CuI (2.6 mg, 13.6 µmol, 0.02 equiv. to **10**) and $Pd(PPh_3)_2Cl_2$ (19.2 g, 27.4 µmol, 0.04 equiv. to **1f**) were added sequentially. The reaction was heated to 60 °C and stirred under N_2 atmosphere for overnight. After the reaction was finished, TEA was evaporated using rotary evaporator. The mixture was diluted with EA and washed with

dilute (1~2 %) HCl DI water solution (150 mL×2) and brine (150mL×1). EA phase was collected and dried over $MgSO_4$. Column chromatography (SiO_2, 0 ~ 80% EtOAC / hexane gradient eluent) gave compound **1g** as thick yellow oil (347 mg). The yellow color was likely due to the metal residual, which can be removed by QuadraPure® TU. ^{1}H NMR (500 MHz, $CDCl_3$): δ 7.17 - 7.15 (d, J = 8.2 Hz, 4H), 6.85- 6.83 (d, J = 8.0 Hz, 4H), 5.35 – 5.31 (m, 2H), 4.37 - 4.36 (m, 2H), 4.16 - 4.05 (m, 4H), 3.80 – 3.74 (m, 6H), 2.66 – 2.63 (t, *J* = 6.2 Hz, 4H), 2.06 – 2.00 (m, 4H), 1.66 – 1.60 (m, 4H), 1.36 – 1.26 (m, 24H). ^{13}C NMR (126 MHz, $CDCl_3$) δ 172.32, 138.70, 131.58, 130.97, 127.85, 121.48, 86.48, 65.64, 61.27, 44.82, 43.48, 32.19, 29.77, 29.54, 29.44, 29.00, 28.77, 28.19, 26.41, 23.96. HRMS-ESI (m/z): $[M + H]^+$ calculated for $C_{46}H_{60}O_6$, 709.4463; observed 709.4467.

Synthesis of 1h. To a 50 mL three-neck RBF charged with a stir bar, compound **1g** (347 mg, 0.49 mmol) was dissolved in 25 mL THF. The solution was purged with N_2 for 10 min. Under nitrogen atmosphere, Pd/C (10% Pd) (30 mg) was added portion-wise. The mixture was purged with N_2 for another 10 min. The hydrogen balloon was connected to the RBF. The mixture was purged with hydrogen for 10 s and was allowed to react under hydrogen atmosphere for 48 h. After the reaction was finished, the solution was filtered with celite. The filtrate was loaded onto silica by rotary-evaporating the solvent. Column chromatography (SiO_2, 0 ~ 80% EtOAC / hexane gradient eluent) gave compound **1h** as thick colorless oil (312 mg). ^{1}H NMR (500 MHz, $CDCl_3$): δ 6.91 – 6.89 (d, J = 7.9 Hz, 4H), 6.82 - 6.81 (d, J = 8.0Hz, 4H), 4.34 - 4.33 (m, 2H), 4.15 – 4.06 (m, 4H), 3.80 - 3.78 (m, 2H), 3.60 – 3.57 (t, J = 6.4 Hz, 4H), 2.51 - 2.48 (t, J = 7.4 Hz, 4H), 1.65 – 1.46 (m, 16H), 1.37 – 1.28 (m, 30H). ^{13}C NMR (126 MHz, $CDCl_3$) δ 172.71, 140.29, 136.37, 128.09, 127.92, 65.32, 62.84, 44.72, 43.63, 35.16, 32.22, 29.21, 29.16, 28.84, 28.72, 28.51, 28.13, 27.65, 27.63, 27.48, 25.90. HRMS-ESI (m/z): $[M + H]^+$ calculated for $C_{46}H_{70}O_6$, 719.5245; observed 719.5249.

Synthesis of 1i. To a 25 mL RBF charged with a stir bar, compound **1h** (312 mg, 0.43 mmol) and DMAP (10 mg, 82.9 μmol) were dissolved in 10 mL DCM. 4-pentenoic anhydride (166.5 μL, 166 mg, 0.91 mmol, 2.1 equiv. to **1h**) was added dropwise. The reaction was stirred overnight. After the reaction was finished, the solution was loaded onto silica by evaporating solvent. Column chromatography (SiO_2, 0 ~ 20% EtOAc / hexane gradient eluent) gave compound **1i** as colorless oil (291 mg). ^{1}H NMR (500 MHz, $CDCl_3$): δ 6.90 – 6.89 (d, J = 7.9 Hz, 4H), 6.83- 6.81 (d, J = 7.9 Hz, 4H), 5.77 - 5.85 (ddt, J = 16.4, 10.2, 6.0 Hz, 2H), 5.06 – 4.79 (m, 4H), 4.33 - 4.34 (m, 2H), 4.15 – 4.06 (qt, J = 10.8, 7.0 Hz, 4H), 4.05 – 4.03 (m, 4H), 3.79 – 3.77 (m, 2H), 2.50 – 2.48 (m, 4H), 2.41 – 2.33 (m, 8H), 1.67 – 1.61 (p, J = 7.0 Hz, 4H), 1.57 – 1.53 (m, 8H), 1.37 – 1.30 (m, 32H). ^{13}C NMR (126 MHz, $CDCl_3$) δ 173.24, 172.67, 139.98, 136.84, 136.50, 128.08, 127.97, 115.61, 65.33, 64.34, 44.67, 43.75, 34.96, 33.69, 29.20, 29.16, 29.02, 28.84, 28.72, 28.51, 28.17, 28.13, 27.65, 27.62, 25.90. HRMS-ESI (m/z): $[M + H]^+$ calculated for $C_{56}H_{82}O_8$, 883.6083; observed 883.6078. $[M + NH_4]^+$ calculated for $C_{56}H_{82}O_8$ 900.6348; observed 900.6342. $[M + Na]^+$ calculated for $C_{56}H_{82}O_8$ 905.5902; observed 905.5900.

Synthesis of 1j. To a 500 mL RBF charged with a stir bar, compound **1i** (291 mg, 0.33 mmol) was dissolved in 200 mL DCM. Grubbs 2nd catalyst (14 mg, 16.5 μmol, 0.05 equiv. to **1i**) was then added. The solution was refluxed overnight and quenched with several drops of vinyl ethyl ether. The solution was loaded onto silica gel by evaporating the solvent. Column chromatography (SiO_2, 0 ~ 20% EtOAc / hexane gradient eluent) gave compound **1j** as colorless

oil (220 mg). ^{1}H NMR (500 MHz, $CDCl_3$): δ 6.88 – 6.85 (m, 4H), 6.80 – 6.77 (m, 4H), 5.46 – 5.39 (m, 2H), 4.33 - 4.32 (m, 2H), 4.16 – 4.07 (m, 4H), 4.03 – 4.00 (m, 4H), 3.82 – 3.80 (m, 2H), 2.50 – 2.47 (t, *J* = 7.2 Hz, 4H), 2.35 – 2.30 (m, 8H), 1.67 – 1.62 (p, J = 7.0 Hz, 4H), 1.57 – 1.45 (m, 8H), 1.37 – 1.30 (m, 32H). ^{13}C NMR (126 MHz, $CDCl_3$) δ 173.19, 172.70, 139.86, 136.30, 129.64, 127.98, 65.34, 64.27, 44.88, 43.19, 34.81, 34.30, 29.21, 29.17, 28.85, 28.73, 28.53, 28.14, 28.01, 27.95, 27.67, 27.64, 27.56, 25.91. HRMS-ESI (m/z): $[M + H]^+$ calculated for $C_{54}H_{78}O_8$, 855.5770; observed 855.5777.

Synthesis of P1. A 2 mL crimp top vial was charged with **1j** (46.3 mg, 0.4 equiv.) and freshly distilled 9-oxabicyclo[6.1.0]non-4-ene (10.4 mg, 0.6 equiv.) under N_2 (g). A stock solution of Grubbs Catalyst 2nd Generation in dry DCM (0.66 mg/mL) was prepared and sparged with N_2 (g) for 10 min. Then, the stock solution (0.1 mL) that contains Grubbs Catalyst (1/1500 equiv.) was added via an air-tight syringe to dissolve the monomers to the concentration of 1 M and initiate the polymerization. After 16 hours, the polymerization was quenched with 5 drops of ethyl vinyl ether and then precipitated into methanol to give the crude polymer. Polymers were purified via two additional precipitations into MeOH and one reverse precipitation from DCM. The polymer was dried on the high vac for at least 1 hour prior to use. ^{1}H NMR (500 MHz, $CDCl_3$): δ 6.90 – 6.88 (m, 4H), 6.83 – 6.81 (m, 4H), 5.51 – 5.44 (m, 4.7H), 4.34 - 4.33 (m, 2H), 4.15 – 4.10 (m, 8H), 3.78 – 3.77 (m, 2H), 2.94 – 2.88 (m, 2.9H), 2.50 – 2.47 (m, 4.3H), 2.36 – 2.12 (m, 13.7H), 1.67 – 1.54 (m, 20H), 1.37 – 1.29 (m, 33H). M_n = 354 kDa, PDI = 1.38.

Single-molecule force spectroscopy of **P1**

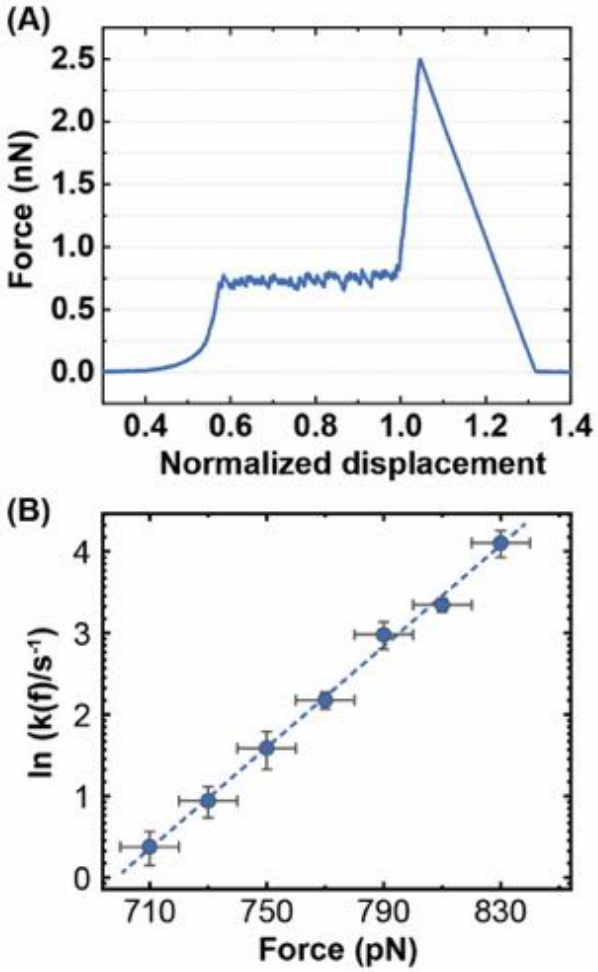

Fig. S1. SMFS characterization of P1. (**A**) A representative force-displacement curve for **P1**. (**B**) Reaction rate-force dependence of **P1** extracted from constant velocity experiment. The dashed line is the linear fitting of the logarithm of the reaction rate as a function of force. Detailed analysis methods have been shown in the previous publication (*2*).

Network preparation

Fresh acrylate monomer was prepared by passing it through a basic aluminum oxide pad to remove the inhibitor before every network preparation. Here we use a pair of elastomers (**E1** and **E2**) with a stoichiometry of [M]:[C]:[CTA]:[PI] = 1: 1/50 : 1/1200 : 1/2000 as an example. Other elastomers were prepared in the same manner. A pre-gel solution was prepared by mixing 2-methoxyethyl acrylate (M) (7g, 1 equiv.), 4-Cyano-4-[(dodecylsulfanylthiocarbonyl)sulfanyl]pentanoic acid (CTA) (18.1 mg, 1/1200 equiv.), and α-ketoglutaric acid (PI) (3.93 mg, 1/2000 equiv.) in a 45 mL scintillation vial. The pre-gel solution was sonicated for 5 min to obtain a homogeneous solution. The pre-gel solution was separately transferred into two 20 mL scintillation vials (3 mL each) with a pipette. The desired amount of different stock solutions of crosslinkers (200 ~ 300 mg/mL) was separately added to these two vials to obtain two solutions with the same ratio of [M] : [C] : [CTA] : [PI] = 1: 1/50 : 1/1200 : 1/2000. Since the stock solution of crosslinkers may have different concentrations, the desired amount of solvent was added to ensure the same concentration for both solutions. These two vials with different crosslinkers were put onto a rotary evaporator to remove the volatile component. Afterward, the solutions were purged with nitrogen for 3 mins. Each solution was passed through a 1 μm pore size PTFE syringe filter to remove dust and transferred into a "sandwich" mold (Fig. S2) using syringes. The molds were placed in a nitrogen-purged glove bag and were irradiated with 365nm UV light (Analytik Jena, UVL-28 UV lamp, 8 Watt) for at least 20 hours to ensure good crosslinking. After crosslinking, the network films were taken out and blown with nitrogen for overnight to remove solvent residue. The dried films were cut into desired shapes for following mechanical tests.

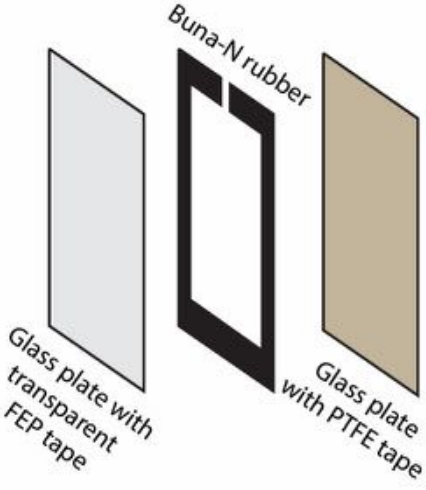

Fig. S2. Mold setup. "Sandwich" mold was made by binding two glass plates and a Buna-N rubber (~0.8 mm thick) spacer together. Inner dimension of the spacer is around 60 × 120 mm (120 mm × 120 mm for the samples for fatigue tests). Low friction transparent FEP tape (~ 0.0035" thick) and PTFE tape (~ 0.012" thick) were applied to the glass plates to help with demolding.

Network characterizations

1) Rheology

Network films were cut to size with an 8 mm diameter biopsy punch. Rheological measurements were conducted on an Anton Paar MCR 302 rheometer with an 8 mm parallel plate geometry. Frequency sweep measurements were conducted at 22-23 °C with a constant 0.5% shear strain, well within the linear viscoelastic regime based on initial strain sweeps. Constant temperature was maintained with a Peltier temperature control stage. Three samples from different positions in the network film were punched out for shear moduli measurement. Frequency sweep data are shown in Fig. S3.

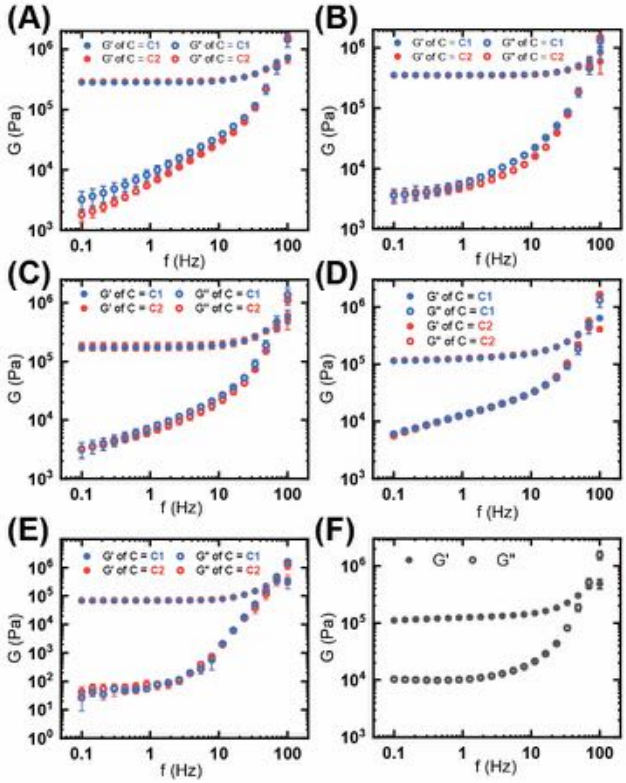

Fig. S3. Frequency sweeps. Elastomers with stoichiometry of (**A**) [M] : [C] : [CTA] : [PI] = 1: 1/50 : 1/300 : 1/1500, (**B**) [M] : [C] : [CTA] : [PI] = 1: 1/50 : 1/300 : 1/1500, (**C**) [M] : [C] : [CTA] : [PI] = 1: 1/100 : 1/1200 : 1/2000, (**D**) [M] : [C] : [CTA] : [PI] = 1: 1/200 : 1/1200 : 1/2000. (**E**) Gels (50% volume fraction) with stoichiometry of [M] : [C] : [PI] = 1: 1/200 : 1/4500. (**F**) Highly entangled polymer with stoichiometry of [M]: [PI] = 1: 10^{-6}. No additional crosslinker or solvent used. Entanglement modulus was taken from the *G'* at 0.1 Hz in fig. F. Error bars are standard deviation.

2) Sol fraction and equilibrium swelling ratio

After rheology tests, the disc samples (×3) were weighted and submerged in ethyl acetate solvent to extract sol fractions. The solvent was changed every 24 hours until the mass of the dry samples stops changing. The mass of the dry samples usually reaches constant after three times of solvent exchange. The sol fractions were calculated by (mass loss)/(initial mass)×100%. The dry samples were then submerged in DMF to reach equilibrium swelling. The equilibrium swelling ratios were calculated by (mass of the swollen sample)/(mass of the dry sample). The results of sol fraction and equilibrium swelling ratios are shown in Fig. S4.

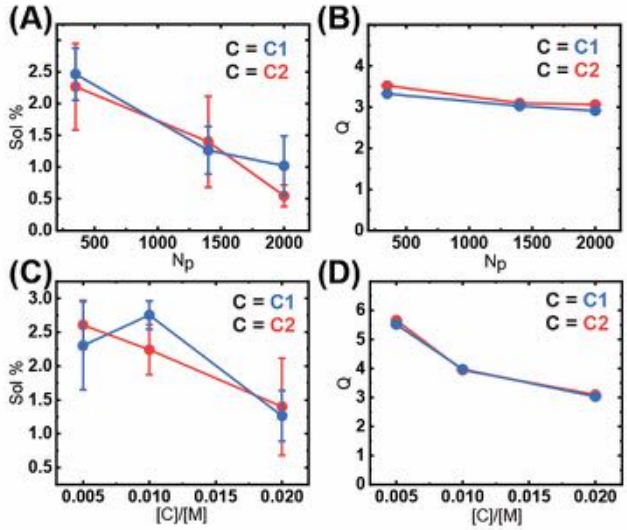

Fig. S4. Sol fractions and equilibrium swelling ratios. (**A**) Sol fractions and (**B**) equilibrium swelling ratios Q of elastomers with [C] : [M] = 1 : 50, and $N_p \approx 350$, 1400, 2000, respectively. (**C**) Sol fractions and (**D**) equilibrium swelling ratios Q of elastomers with $N_p \approx 1400$, [C] : [M] = 1 : 200, 1 : 100, 1 : 50. Error bars are standard deviation.

3) Differential Scanning Calorimetry (DSC)

DSC measurements were performed using a TA instrument (DSC2500). The sample of 4 ~ 8 mg was placed in a non-hermetic pan, and an empty pan was used as a reference pan. The DSC experiment was performed in a heat-cool cycle, samples of **E1** and **E2** were performed following this procedure (-50 ℃ to 50 ℃, 10 ℃/min; isothermal 50 ℃, 3 min; 50 to -50 ℃, 10 ℃/min; isothermal -50 ℃, 3 min; -50 ℃ to 50 ℃, 10 ℃/min; isothermal 50 ℃, 3 min; 50 to -50 ℃, 10 ℃/min), wherein the thermal transitions for the heating cycle were recorded. The glass transition temperature (T_g) was determined by the inflection point of the heat capacity with temperature sweep (second cycle). The T_g of **E2** is consistent with reported data (*31*) of linear poly 2-methoxyethyl acrylate, where T_g of **E1** is slightly higher, but still well below room temperature (Fig. S5).

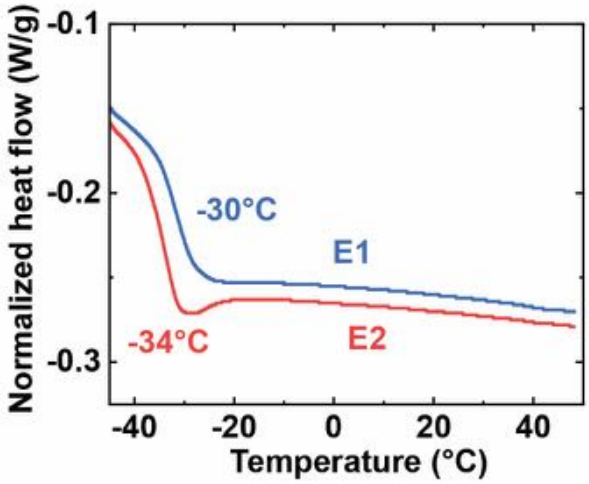

Fig. S5. DSC measurement of E1 and E2. The glass transition temperature of **E1** is about 4 degrees Celsius higher than that of **E2**, but both of them are well below room temperature, at which mechanical tests were performed.

4) Tearing energy and fatigue threshold

The fatigue tests were conducted following the previous method (*1*). Samples for tearing energy were cut with a razor blade as a 15 × 20 mm rectangle. This was reduced to a 20 × 3 mm area after clamping. Typically, each measurement used 3 un-notched samples and 5 notched samples; for notched samples, a ~ 5 mm cut was made in the center of one side of the piece, perpendicular to the edge. The exact thickness and width were measured with calipers before each test. Samples were loaded into the clamps at a gauge length of ~2 mm, then stretched to a force of about 0.01 N, which resulted in an initial gauge length of 2.5 ± 0.5 mm. Unnotched samples and notched samples were pulled to failure at a constant strain rate of 0.2%. Tearing energy was calculated using the Rivlin-Thomas method (*7*) where the strain energy is obtained by integrating the un-notched stress-strain curve to the strain at which the crack of the notched samples began to propagate. Results are shown in Fig. S6 and Table S1.

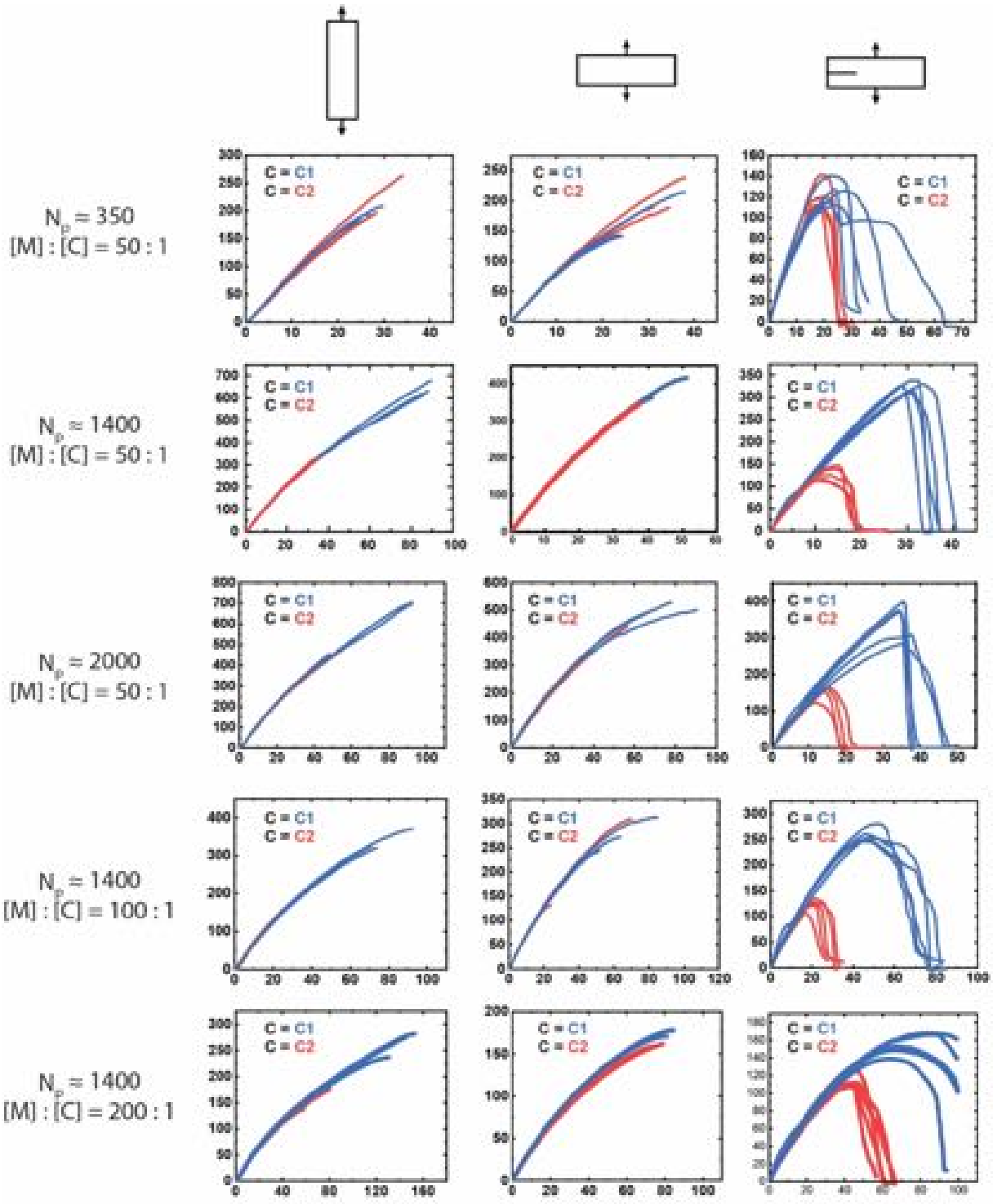

Fig. S6. Stress-strain curves for different geometries. Columns are different sample geometries: rectangle tensile, pure shear tensile, and pure shear fracture. Rows are the same samples tested under these geometries. The information of tested samples is shown at the beginning of each row. For each plot, the y-axis is the stress in kPa, the x-axis is the strain in %.

Table S1. Summary of tearing energies for elastomers in Fig. S6. Blue and red color indicates the tearing energies for elastomer made from **C1** and **C2**, respectively. The values are mean ± standard deviation.

N_p \ [M] : [C]	200 : 1	100 : 1	50 : 1
350	-	-	$21.9 \pm 4.9\ J \cdot m^{-2}$ $15.6 \pm 5.6\ J \cdot m^{-2}$
1400	$248.3 \pm 16.6\ J \cdot m^{-2}$ $66.7 \pm 5.2\ J \cdot m^{-2}$	$148.6 \pm 3.2\ J \cdot m^{-2}$ $23.7 \pm 3.1\ J \cdot m^{-2}$	$113.0 \pm 9.7\ J \cdot m^{-2}$ $11.5 \pm 3.7\ J \cdot m^{-2}$
2000	-	-	$135.8 \pm 11.6\ J \cdot m^{-2}$ $19.8 \pm 4.1\ J \cdot m^{-2}$

The fatigue tests were conducted based on a method described by Suo, Zhao, and coworkers (*9,17*). Samples for the fatigue test were cut with a razor blade as a 30 mm × 30 mm rectangle. This was reduced to around 30 × 3 mm area after clamping. Acrylic sheets and Buna-N rubber spacers were used to achieve a wide and firm grip for these samples (Fig. S7). A ruler tape is attached to the acrylic grip. Each measurement used 3 un-notched samples to obtain uniaxial tensile stress-strain curves. For notched samples, a ~ 5 mm cut was made in the center of one side of the piece, perpendicular to the edge. These samples were subjected to a displacement-controlled cyclic load with a frequency of 1 Hz at a constant displacement rate. The crack propagation was monitored with a webcam (Logitech HD Pro C920), which takes a photo of the sample every second. Based on the photos, the growth of crack length c per cycle (dc/dN) can be estimated. For samples that do not have observable crack propagation, a thousand cycles were applied at least. The energy release rate was calculated by integrating the un-notched stress-strain curves to the strain applied and multiplying it with the initial height of the sample. With these data, dc/dN against the energy release rate can be plotted (Fig. 2G-H).

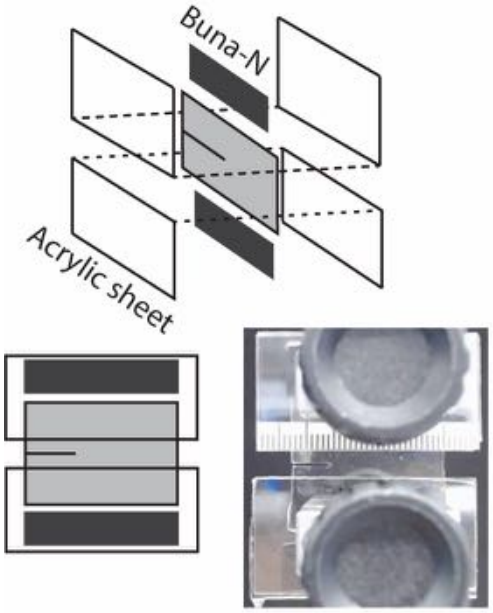

Fig. S7. Sample setup for fatigue tests. Two acrylic sheets on each side were used to achieve wide and firm grip of the elastomer film. Buna-N rubber was used between two acrylic sheets as a spacer.

Fracture of gels prepared at 50% volume fraction

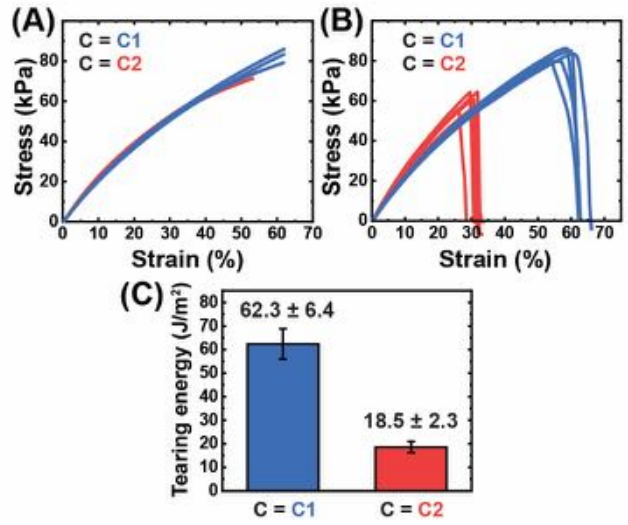

Fig. S8. Stress-strain curves of un-notched and notched gels. Gels were prepared at 50% volume fraction (propylene carbonate as solvent) with a stoichiometry of [M] : [C] : [PI] = 1: 1/200 : 1/4500 without CTA. (**A**) Pure shear tensile test. (**B**) Pure shear tearing test. (**C**) Tearing energies comparison.

Elastomers made from ethyl acrylate

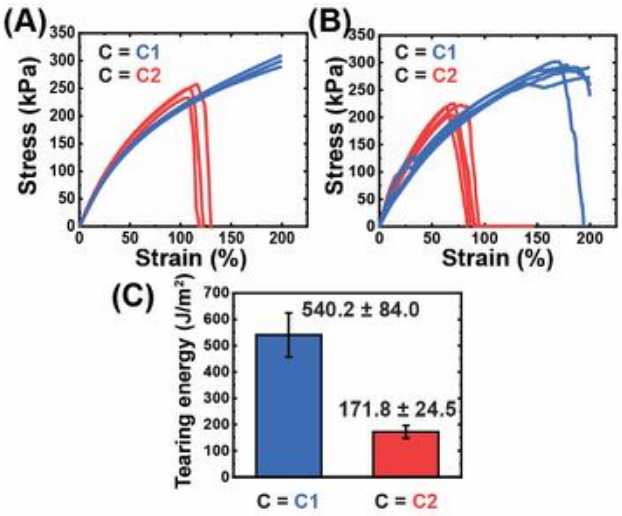

Fig. S9. Stress-strain curves of un-notched and notched ethyl acrylate elastomer. Elastomers were prepared with a stoichiometry of [M] : [C] : [CTA] : [PI] = 1: 1/200 : 1/1200 : 1/2000. Ethyl acrylate was used as the monomer instead of 2-methoxyethyl acrylate. (**A**) Pure shear tensile test. (**B**) Pure shear tearing test. (**C**) Tearing energies comparison.

Elastomers made from "intermediate" crosslinker **C3**

Results in main text suggest that the crosslinker needs to be weaker than the primary chain to achieve this toughening effect, but we wonder what the relative strength between the crosslinker and the primary chain could give maximum effect. We synthesized an "intermediate" crosslinker **C3** (synthesis of **C3** is shown in section chemical synthesis) based on a precursor of **C1**. Albeit no direct SMFS characterization on this specific cyclobutane, similar *cis*-diester substituted cyclobutanes characterized by SMFS show activation forces of ~ 2 nN on the timescales of milliseconds (*32*), making **C3** still a preferential site for breaking in networks compared to the primary chains. Elastomer **E3** was made from **C3** in the same way as **E1** and **E2**, and they have similar shear moduli and stress-strain curves (Fig. S10B). However, the tearing energy of **E3** (19.3 ± 5.5 J · m^{-2}) is only slightly larger than that of **E2** and much smaller than that of **E1**. Therefore, to achieve a significant enhancement in tearing energy, the crosslinker is not just required to be mechanochemically weak, but it has to be at least two times weaker than the primary chain. Another extreme would be the case when the crosslinkers require zero force to break (no crosslinker), which clearly cannot toughen the network as the polymer melt synthesized at the same condition flows instead of fractures. With the same primary chain length and crosslinking density, we expect an optimal activation force for the crosslinkers that can provide the most significant toughening effect, but it requires a more sophisticated design of the crosslinker to achieve.

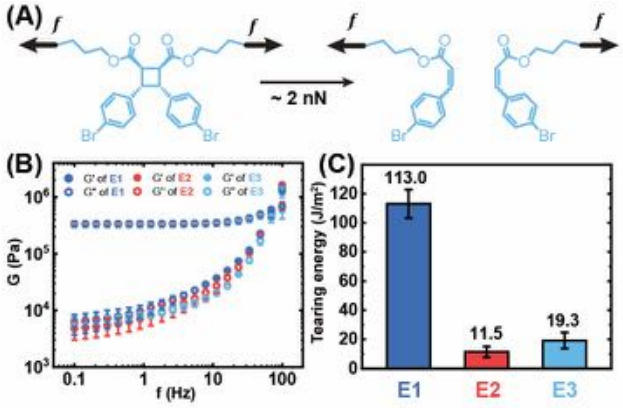

Fig. S10. Elastomer E3 made from intermediate crosslinker C3. Elastomers are prepared with a stoichiometry of [M] : [C] : [CTA] : [PI] = 1: 1/50 : 1/1200 : 1/2000. (**A**) Force-trigger cycloreversion of "intermediate" crosslinker **C3**. (**B**) Frequency sweep of **E1-3**. (**C**) Tearing energies of **E1-3**. The T-test between **E2** and **E3** shows a p-value of $p = 0.089 > 0.05$, indicating the tearing energy of **E3** is not significantly larger than **E2**.

Degree of polymerization of primary chains N_p in elastomers

To show that the chain transfer agent has good control over the molecular weight of primary chains in the networks, we performed an experiment shown in Fig. S11. Same pre-gel solution was separately polymerized with an acid-degradable crosslinker **C4** and same amount of additional monomer, such that the concentration of acrylate groups are identical in these two mixtures. Polymerization were performed in the same way described in section of network preparation. Polymer **PA1** was polymerized without crosslinker, polymer **PA2** was obtained by first forming elastomer **E4** and then degrading the crosslinkers. After polymerization, 200 mg **PA1** and 200 mg **E4** were separately submerged and stirred in a solution containing trifluoroacetic acid (TFA) (100 μL) and methanol (200 μL) in 10 mL THF. Elastomer **E4** first swelled to equilibrium and degraded within 5 hours. After 24 hours, PA1 and PA2 were obtained by extracting with EA and washing with water.

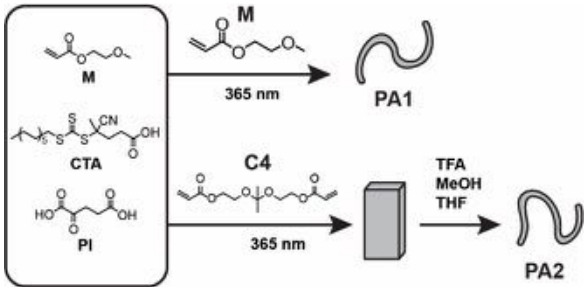

Fig. S11. Synthesis of PA1, E4 and PA2. Elastomers with **C4** were prepared with four stoichiometries, [M] : [CTA] = 400 : 1, 600 : 1, 1200 : 1, and 3600 : 1. Four corresponding PA1 were prepared as well. [M] : [C] was fixed at 50 : 1.

GPC traces of **PA1** and **PA2** prepared with 4 different stoichiometries are shown in Fig. S12. When [M]/[CTA] ≤ 1200, CTA has good control over the molecular weights of primary chains (solid and dashed lines are almost overlapped for red, blue, and black). When [M]/[CTA] = 3600, the **PA2** synthesized from degrading the network has a retention time longer than **PA1** synthesized without crosslinkers (green).

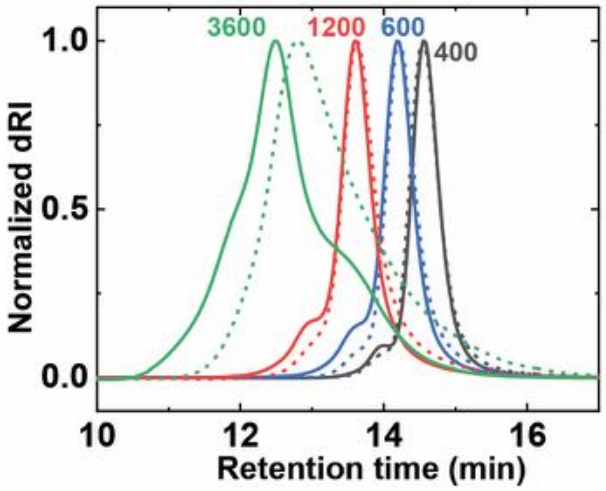

Fig. S12. GPC traces for PA1 and PA2. PA1 are shown in solid lines and **PA2** are shown in dashed lines. Numbers and colors indicate the different ratios [M]/[CTA] used during preparation.

Elastomers reported in Fig. 3C-F&S6 and Table S1, were prepared at three different [M] : [CTA] ratios, which are 300 : 1, 1200 : 1, and 3600 : 1. We used the same pre-gel solution and prepared **PA1** and **PA2** in parallel with **E1** and **E2**. Based on Fig. S12, we used the molecular weight of **PA1** as an estimate for N_p when [M]/[CTA] ≤ 1200, and we use the molecular weight of **PA2** to estimate N_p when [M]/[CTA] = 3600. In the end, three different [M] : [CTA] ratios resulted in $N_p \approx$ 350, 1400, and 2000, respectively. GPC traces for the primary chains that were used for N_p estimation are shown in Fig. S13. A summary of molecular weights and estimated N_p are shown in Table S2.

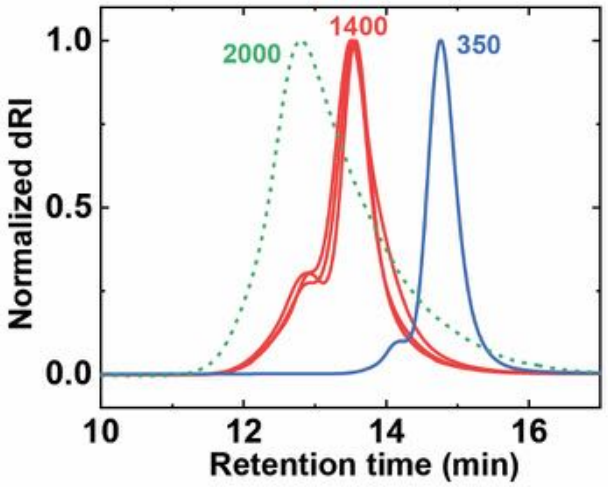

Fig. S13. GPC traces for N_p estimation. For [M]:[CTA] = 300 and 1200 (blue and red), the corresponding **PA1** (solid lines) were used to estimate N_p. For [M]:[CTA] = 3600 (green), the corresponding **PA2** (dashed line) was used to estimate N_p.

Table S2. Summary of N_p estimation for elastomers in Fig. 3 and Fig. S6. Data shaded with blue, red, green colors correspond to the blue, red, and dashed green traces shown in Fig. S13.

[M]:[C] / [M]:[CTA]	200 : 1	100 : 1	50 : 1
300	-	-	M_n = 45.0 ± 0.9 kDa $N_p \approx$ 350
1200	M_n = 207.9 ± 8.3 kDa $N_p \approx$ 1590	M_n = 163.2 ± 3.2 kDa $N_p \approx$ 1260	M_n = 174.1 ± 3.5 kDa $N_p \approx$ 1340
3600	-	-	M_n = 260 ± 14 kDa $N_p \approx$ 2000

Thermal stability of **E1**

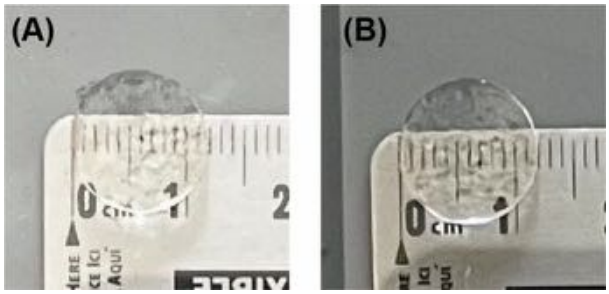

Fig. S14. Thermal stability of E1. (**A**) **E1** was submerged in DMF and reached equilibrium swelling. (**B**) **E1** was heated to 100 °C in DMF solvent for 96 hours and cooled down to room temperature. No further swelling was observed, indicating crosslinker **C1** remained stable under this condition.

Molecular dynamic simulation of tensile fracture

General simulation details. The Large-scale Atomic/Molecular Massively Parallel Simulator (LAMMPS) package (*33*) was used with the coarse-grained bead-spring model (*34*, *35*) of polymer chains. Monomers (beads) are interacting via the Lennard-Jones (LJ) potential (*36*, *37*)

$$U_{LJ}(r;r_c)=\begin{cases}4\varepsilon\left[\left(\frac{\sigma}{r}\right)^{12}-\left(\frac{\sigma}{r}\right)^{6}-\left(\frac{\sigma}{r_c}\right)^{12}+\left(\frac{\sigma}{r_c}\right)^{6}\right] & r\le r_c\\ 0 & r>r_c\end{cases} \quad \text{(S1)}$$

where the LJ interaction is truncated at $r_c = 2.5\sigma$. We set $\varepsilon = 1kT$, which corresponds to non-solvent condition of implicit solvent. Bonded interactions are modeled by the Finite Extensible Nonlinear Elastic (FENE) potential (*35*)

$$U_{FENE}(r)=\begin{cases}-\frac{1}{2}KR_0^2\,ln\left[1-\left(\frac{r}{R_0}\right)^2\right] & r\le R_0\\ \infty & r>R_0\end{cases} \quad \text{(S2)}$$

with a spring constant $K = 30\ kT\sigma^{-2}$, and a cutoff distance $R_0 = 1.5\sigma$. The total bond interaction potential also includes a purely repulsive LJ term,

$$U_b(r)=U_{FENE}(r)+U_{LJ}(r;r_c) \quad \text{(S3)}$$

where the LJ cutoff is $r_c = 2^{1/6}\sigma$.

In all simulations, the pressure was held constant (at $P = 0$) using the Nosé-Hoover barostat with a damping parameter of $100\ \tau_{LJ}$. The temperature was held constant ($kT = 1$ in Lammps units) using the Nosé-Hoover thermostat with a damping parameter of $10\ \tau_{LJ}$. All molecular dynamics simulations were performed with an integration time-step of $0.01\ \tau_{LJ}$.

Network Formation. A precursor melt of $M = 400$ chains with $n = 64$ beads each was equilibrated in the NPT ensemble with $P = 0$ by simulating a long trajectory, $10^6\tau_{LJ}$, which corresponds to $\sim 10^2\tau_R$, where $\tau_R \sim 10^4\tau_{LJ}$ is the relaxation time of a chain (*38*). The equilibrated melt simulations were instantaneously randomly crosslinked emulating gamma irradiation crosslinking.(*39*, *40*) A snapshot of the equilibrated melt was vulcanized by randomly selecting and bonding monomer pairs at a distance below 1.3σ, which corresponds to the first peak in the melt radial distribution function. The extent of reaction of this vulcanization process was $p = 0.1$. The only restriction imposed on the selection of pairs of monomers for bonding was to exclude any monomers at a curvilinear distance of $s = 1,2$ bonds away from an existing crosslinked monomer, thereby setting the minimal strand length to 2 and the minimum loop length to 4. The networks were equilibrated for $10^5\tau_{LJ}$at the NPT ensemble at $P = 0$, followed by a production run of $9 \cdot 10^5\tau_{LJ}$. The average size of the simulation box was determined from the production run and used for the ensuing pulling simulations.

Network topology. The analysis of the vulcanized network topology was carried out using our in-house code that is based on the analogy between elasticity and electrical resistivity.(*41*) The network is mapped onto a network of nodes (formed by two monomers bonded by a crosslink) and edges (all strands connected to these nodes). The NetworkX python package(*42*) is used for identifying the basis set of loops describing the network(*43*). In the following step, the network is

modeled as a collection of resistors (resistivity of strands is proportional to N_x^{-1}) connected at nodes (crosslinks). The voltage of one strand in the largest loop is then set to some finite values and the Kirchhoff circuit laws are then applied by requiring 1) the sum of all currents passing through a node to be zero, and 2) the voltage difference along any closed loop is zero. The numerical solution of this set of equations yields the current in each strand in the network, whereby we identify those strands that carry current as elastically active strands.
We applied the topology analysis to the network formed by random crosslinking as described above. The gel fraction of this network is over 99%, with 66% of the mass being elastically active. The average length (i.e., number of bonds) of the elastically active strands is $\langle N_x \rangle$ = 11.7.

Calibrating breakable bonds. In the bond scission simulations, the unbreakable FENE bond potentials were replaced by the Morse potential(*44*) for the breakable bonds,

$$U_{morse}(r) = D_e\left(1 - e^{-a(r-r_e)}\right)^2 \tag{S4}$$

where the parameters D_e determines the energy of dissociation, r_e is the equilibrium bond length and a controls the width of the potential. We choose $D_e = 120kT$ for the strong bonds and $D_e = 30kT$ for the weak bonds following the experimental system where the strength of the strong and weak bonds differs by a factor of ~ 4. To keep the equilibrium properties of the bonds the same upon switching from unbreakable to breakable bonds, the parameters of the Morse potential were calibrated to match the FENE potential used in the preparation of the networks, Eq. S3. The parameters

$$r_e = 0.96\sigma, \quad a = \sqrt{\frac{31.52}{2D_e}} \tag{S5}$$

were chosen to match the equilibrium length and the local stiffness around the equilibrium of the FENE potential (second derivative of bond potential at equilibrium length $U''(r_e)$). The bonded potentials we used are shown in Fig. S15, comparing the FENE and Morse potentials.
We simulate two networks with these two bond potentials: (i) A strong crosslinker network with both primary chain bonds and crosslinker $D_e = 120kT$; (ii) A weak crosslinker network with primary chain bonds having $D_e = 120kT$ and crosslinker $D_e = 30kT$.

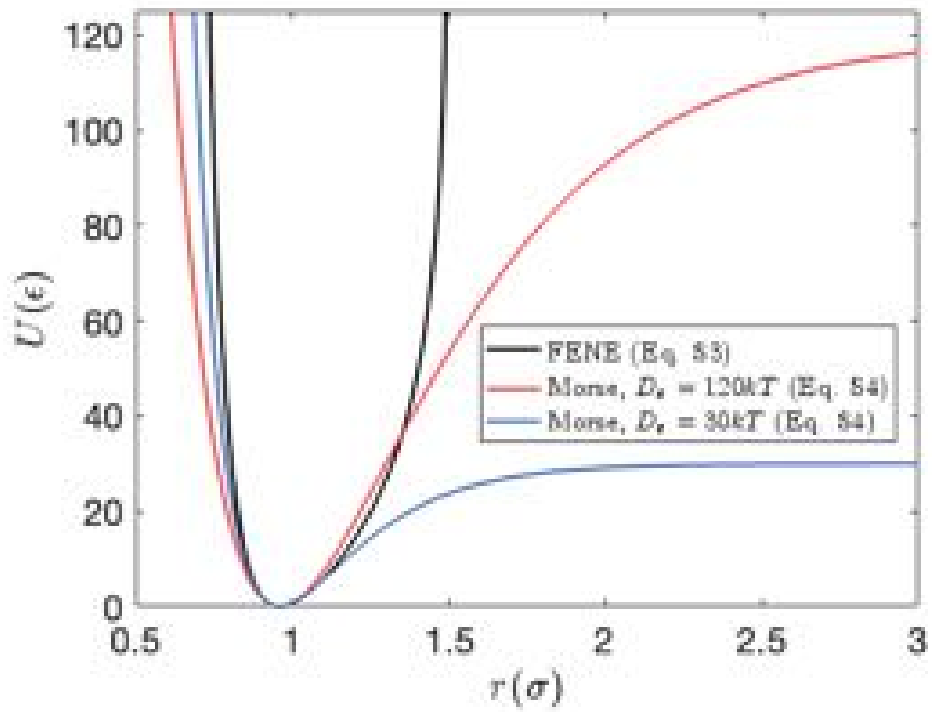

Fig. S15. Bond potentials used in simulations. The FENE bond potential (black curve) is used for equilibrating melts and networks. The Morse potential (red for strong bonds and blue for weak bonds) is used for pulling simulations where bond rupture is desired.

Simulations of bonds scission upon uniaxial extension. The equilibrated networks are uniaxially stretched by changing the z dimension of the simulation box, L_z, from its unperturbed average size, $L_{z,0}$, while the other two dimensions are relaxed at zero pressure by the Nosé-Hover barostat. This mimics the strain-control uniaxial stretching experiments. The network is stretched at a constant strain rate of $10^{-5}\tau^{-1}$ up to the strain $\left(L_z - L_{z,0}\right)/L_{z,0} = 6$. As shown in Fig. S16, the bond scission in weak crosslinker network (blue) almost exclusively occurs at crosslinkers (blue dashed line), while the primary chain bonds are mostly intact (blue solid line). This effect is not observed in the strong crosslinker network (red), in which the primary chain bonds (red solid line) break much more than the crosslinker bonds (red dashed line).

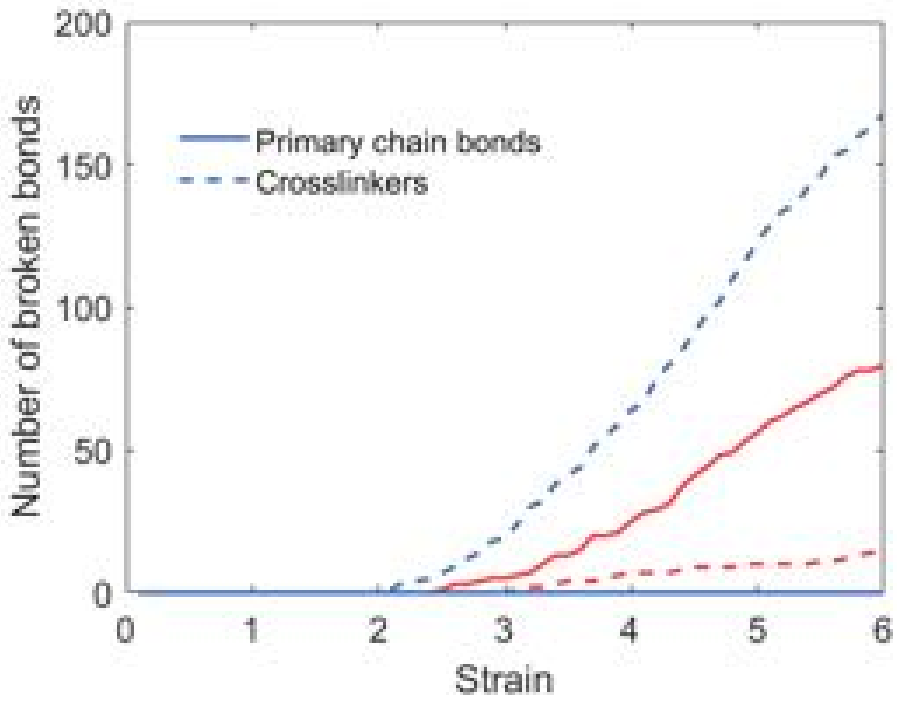

Fig. S16. Number of bonds broken in the network. Red curves represent the strong crosslinker network and blue curves represent the weak crosslinker network. Solid lines – broken primary chain bonds and dashed lines – broken crosslinkers. Blue solid line coincides with horizontal axis as no primary bonds are broken in weak crosslinker network, while in strong crosslinker network most broken bonds are belong to primary chains.

Effect of bond breaking. We show the effect of breaking a bond on the change of average strand lengths $\langle \Delta N_{x,neigh} \rangle$ that are affected by the bond rupture event (neighboring strands of a broken bond). If the broken bond is a crosslinker, the neighboring strands are defined as the four strands it is connected to. If the broken bond is a primary chain bond, the neighboring strands is defined as the strand it is located on and all other strands directly connected to this strand. The definition of neighboring strands associated with a broken bond is shown in Fig. S17 (crosslinkers) and Fig. S18 (primary chain bonds) for different scenarios. As shown in Fig S19, in a weak crosslinker network where the broken bonds are all crosslinkers, the number of elastically inactive strands does not change, while the elastically active strands are combined into longer strands, and their number decreases. In contrast to this result, for the strong crosslinker network where the broken bonds are dominated by the primary chains, the overall effect is an increase in the number of inactive strands and a decrease in the number of active strands as elastically active strands are broken into elastically inactive strands.

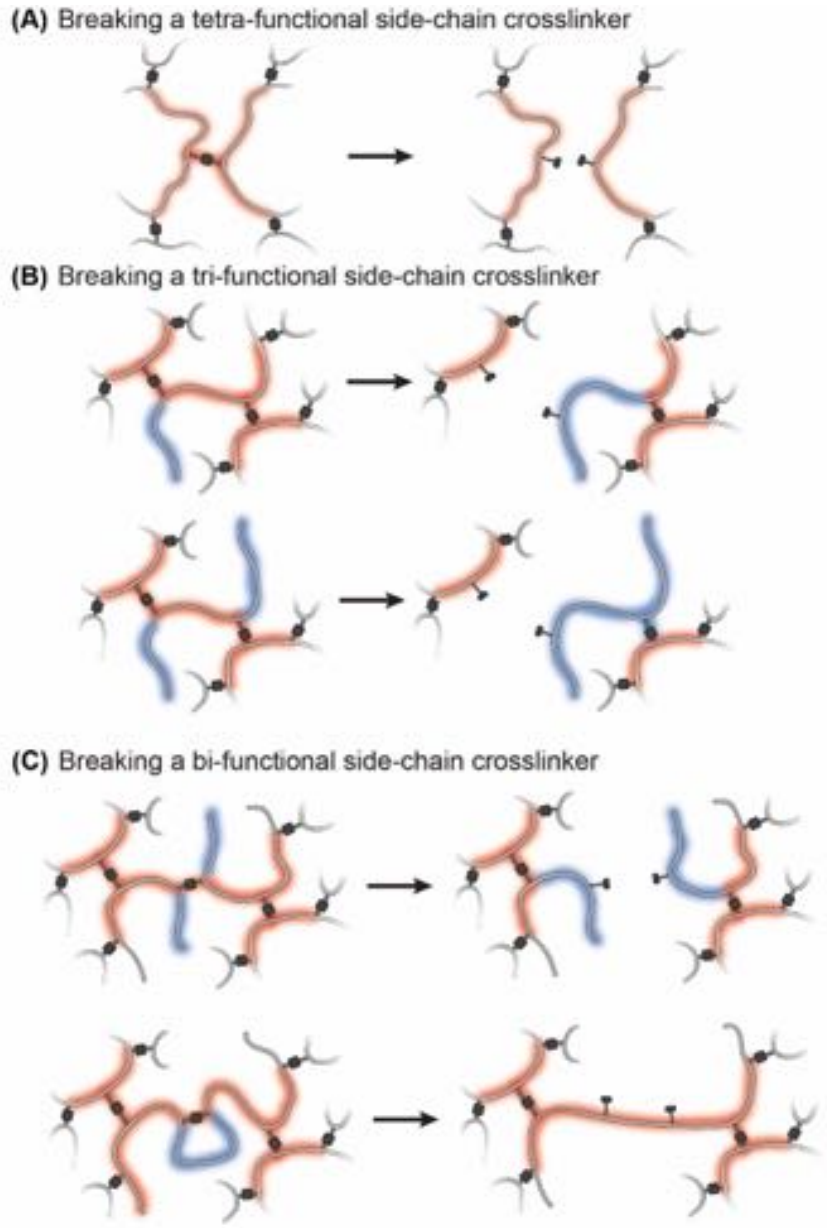

Fig. S17. Schematic illustrations for different scenarios when breaking a crosslinker. Strands colored in red are the neighboring strands associated with breaking a crosslinker. Strands in blue color represents elastically inactive strands. Note that these structures are local structures only. Different strands could belong to the same primary chain.

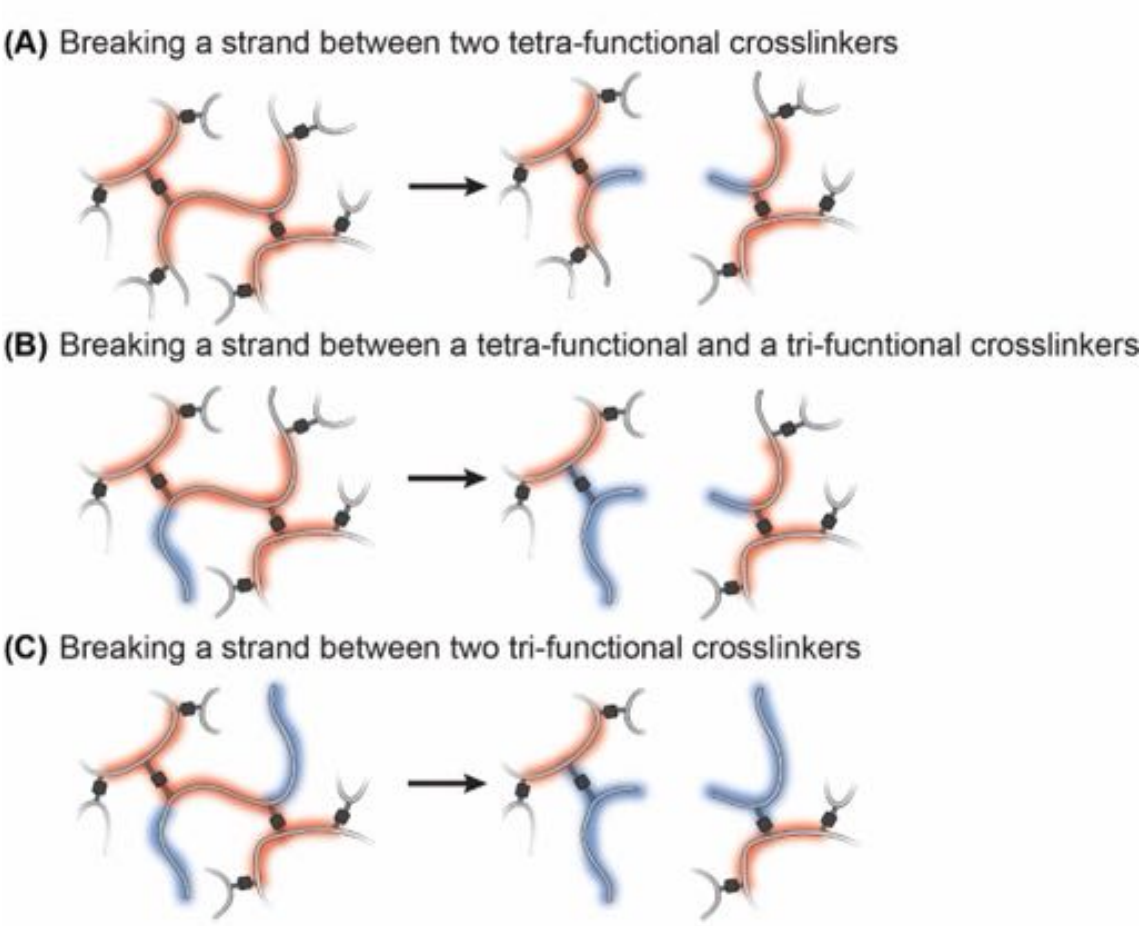

Fig. S18. Schematic illustrations for different scenarios when breaking a primary chain bond. Strands colored in red are the neighboring strands associated with breaking a crosslinker. Strands in blue color represents elastically inactive strands. Note that these structures are local structures only. Different strands could belong to the same primary chain.

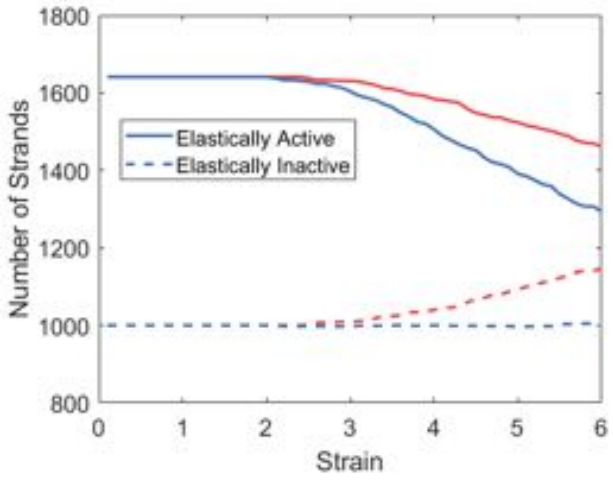

Fig. S19. Number of elastically active and elastically inactive strands as the network is uniaxially stretched. The red curves represent the data for the strong crosslinker network, and the blue curves represent the data for the weak crosslinker network.

The distinct effect of breaking either primary chain bonds or crosslinkers and the dominance of these two types of bonds breakage (primary chain bonds or crosslinkers, Fig. S15) in the two types of networks leads to different modifications on the network topology after bond breaking. Fig. S20 shows the change in average neighboring strand length $\langle \Delta N_{x,neigh} \rangle$ due to a broken bond. For the weak crosslinker network, the change of neighboring strand length is about the average strand length of the network $\langle N_x \rangle$, while the change in the strong crosslinker network is only $\sim \langle N_x \rangle / 5$. It is expected that these effects will be magnified for the bridging strand near the crack tip where multiple crosslinkers on its primary chain could break and its length grows by $\langle N_x \rangle$ for every broken crosslinker. According to the Lakes-Thomas theory, the fracture energy is proportional to the length of these bridging strands. Therefore, we expect that the fracture energy of the weak crosslinker network will be increased by breaking crosslinkers in comparison to the strong crosslinker network where the breaking bridging strands are relatively shorter $\sim \langle N_x \rangle$.

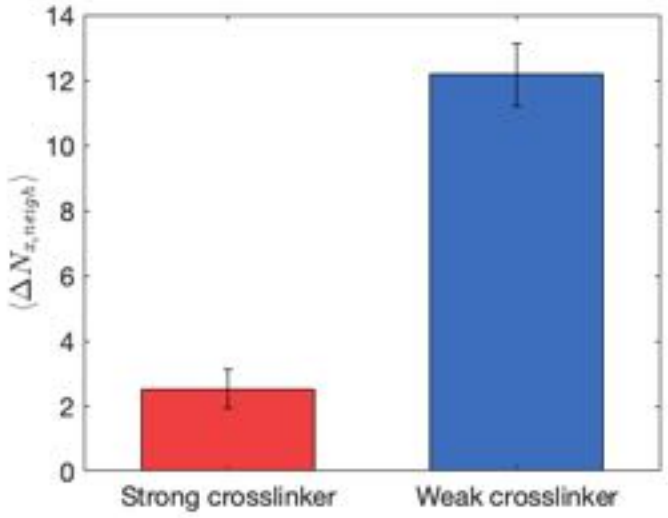

Fig. S20. Increase of average neighboring strand length per scission event at strain of 6. Red column represents the strong crosslinker network and blue column represents the weak crosslinker network.

NMR spectra

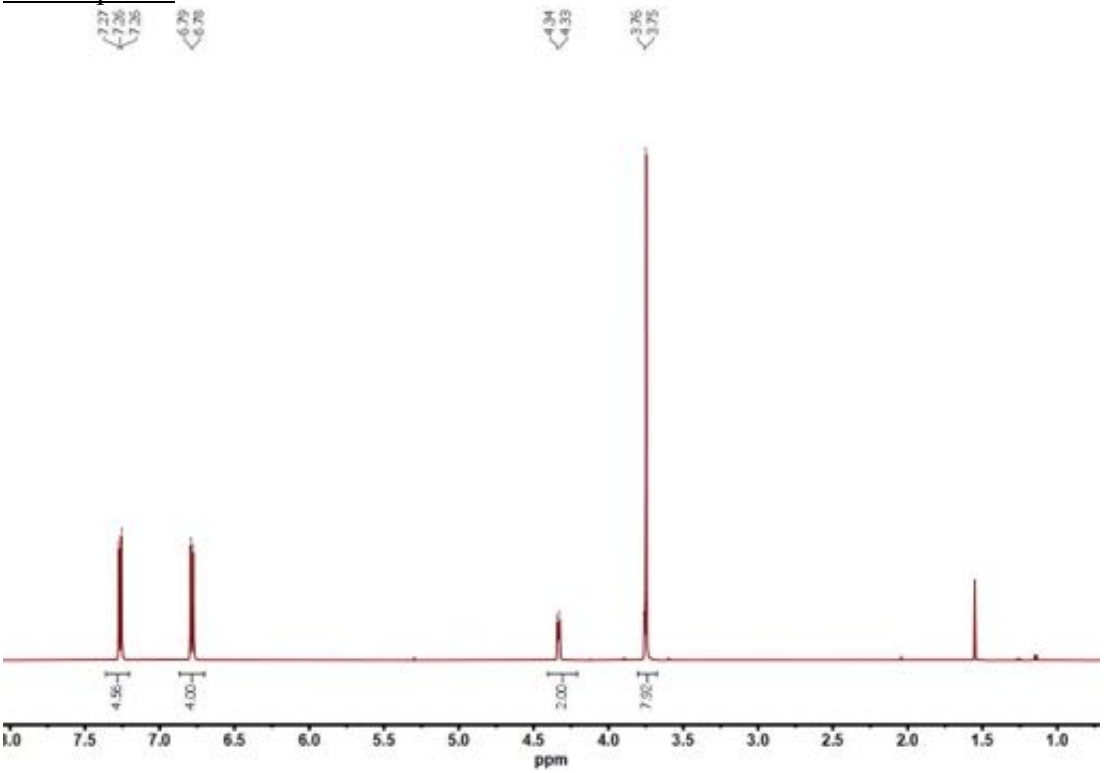

^{1}H NMR (500 MHz, $CDCl_3$) spectrum of **1b**

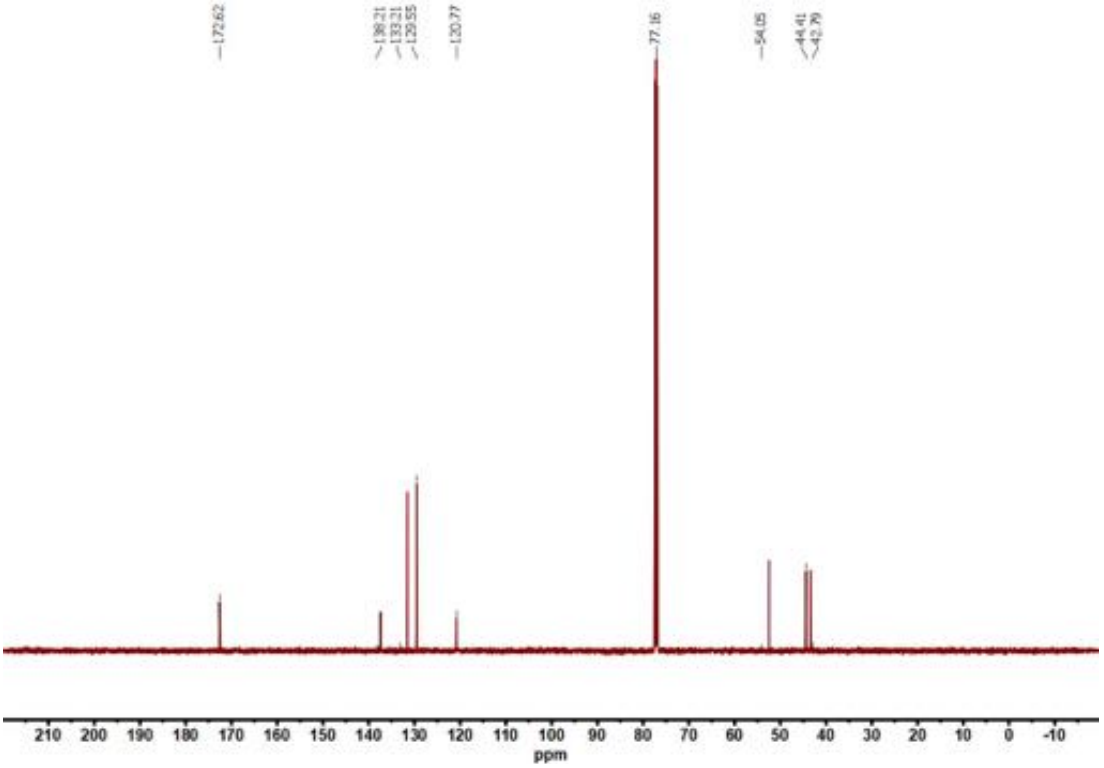

^{13}C NMR (126 MHz, $CDCl_3$) spectrum of **1b**

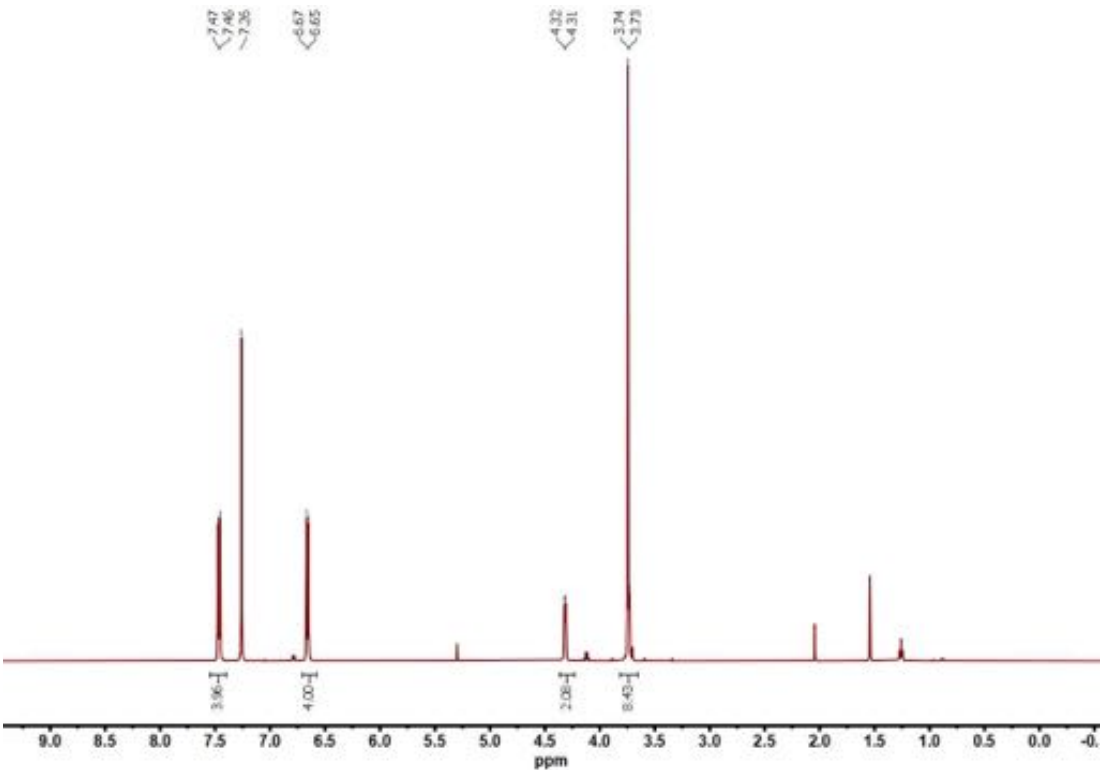

^{1}H NMR (500 MHz, $CDCl_3$) spectrum of **1c**

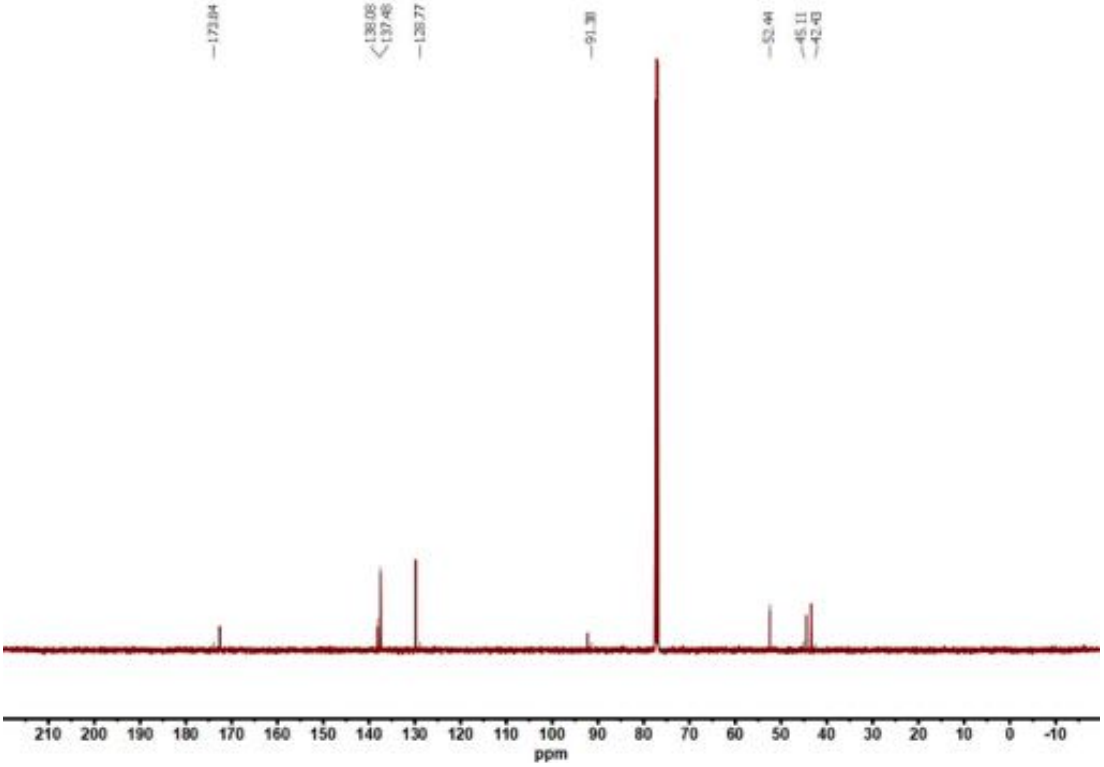

^{13}C NMR (126 MHz, $CDCl_3$) spectrum of **1c**

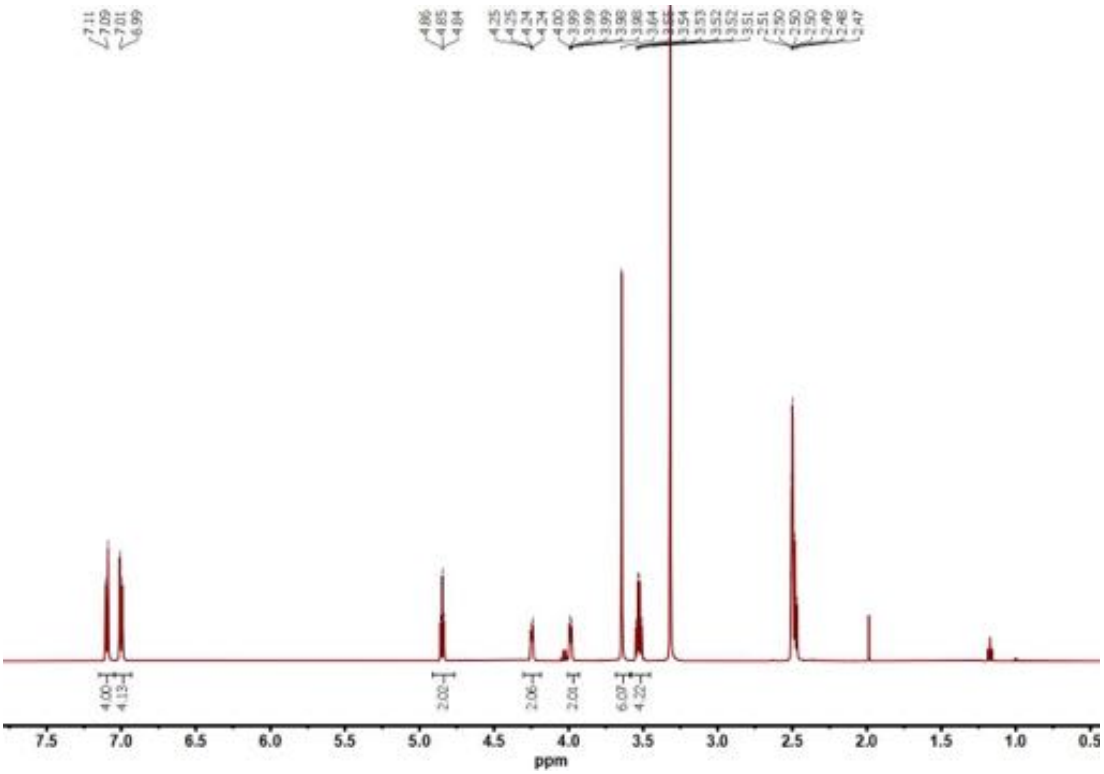

^{1}H NMR (500 MHz, DMSO) spectrum of **1d**

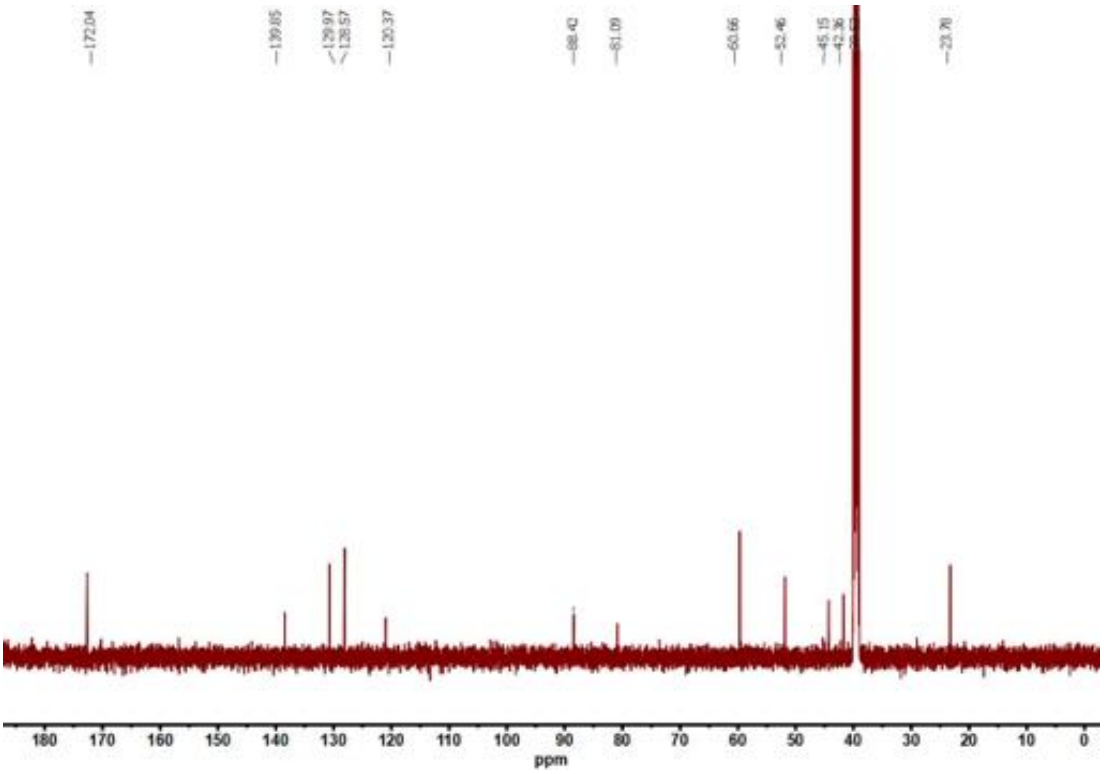

^{13}C NMR (126 MHz, DMSO) spectrum of **1d**

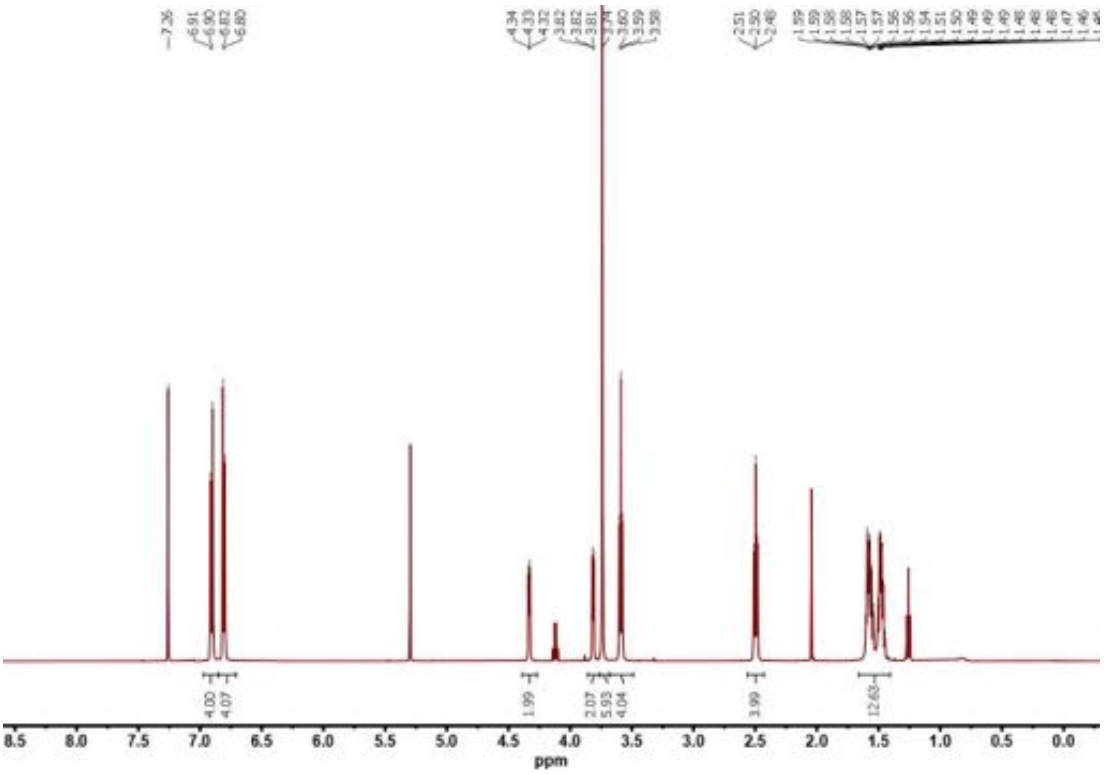

^{1}H NMR (500 MHz, $CDCl_3$) spectrum of **1e**

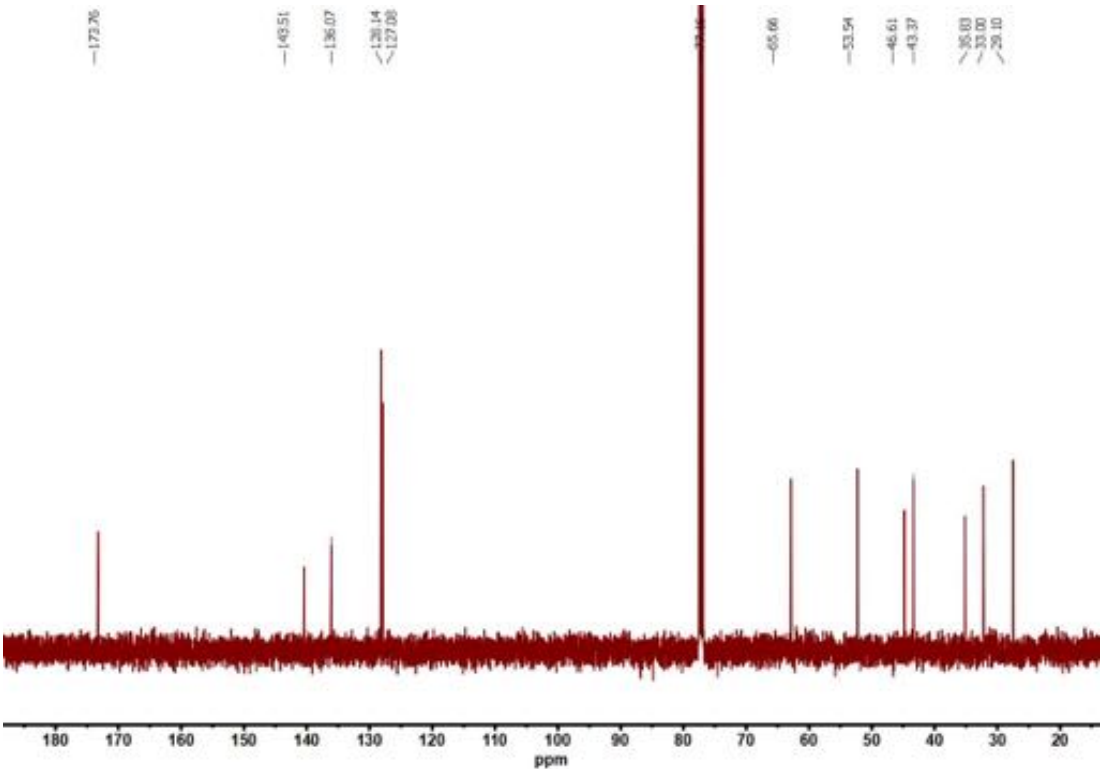

^{13}C NMR (126 MHz, $CDCl_3$) spectrum of **1e**

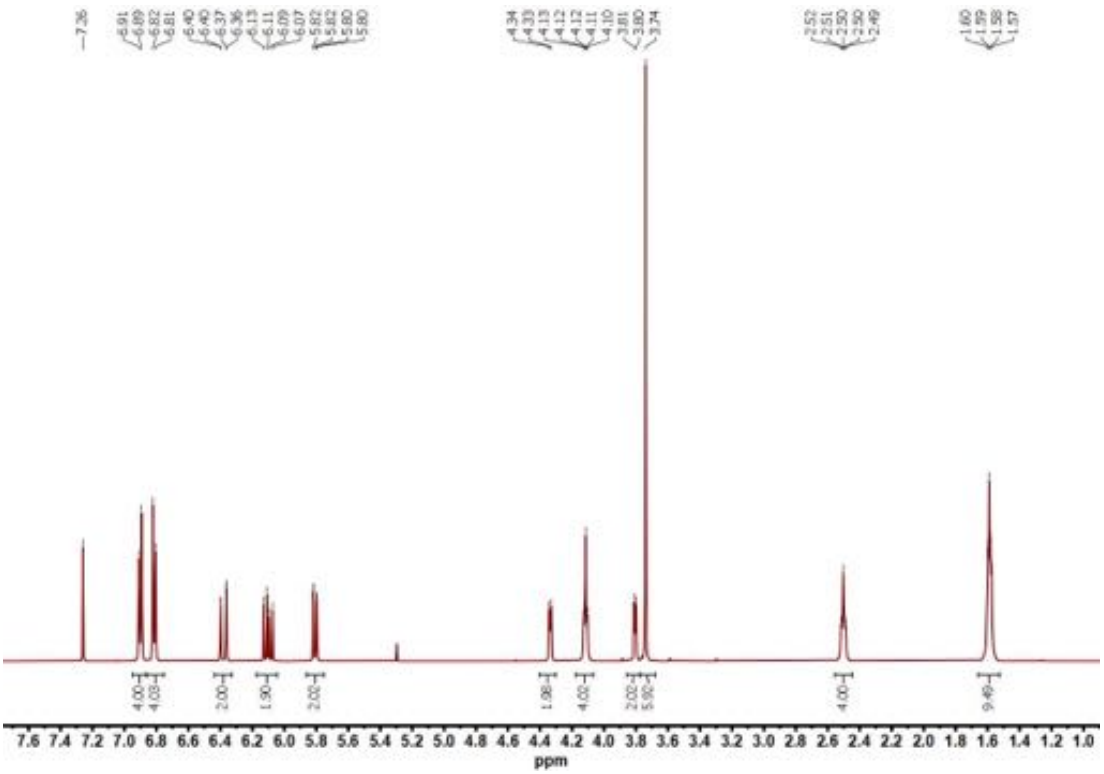

^{1}H NMR (500 MHz, $CDCl_3$) spectrum of **C1**

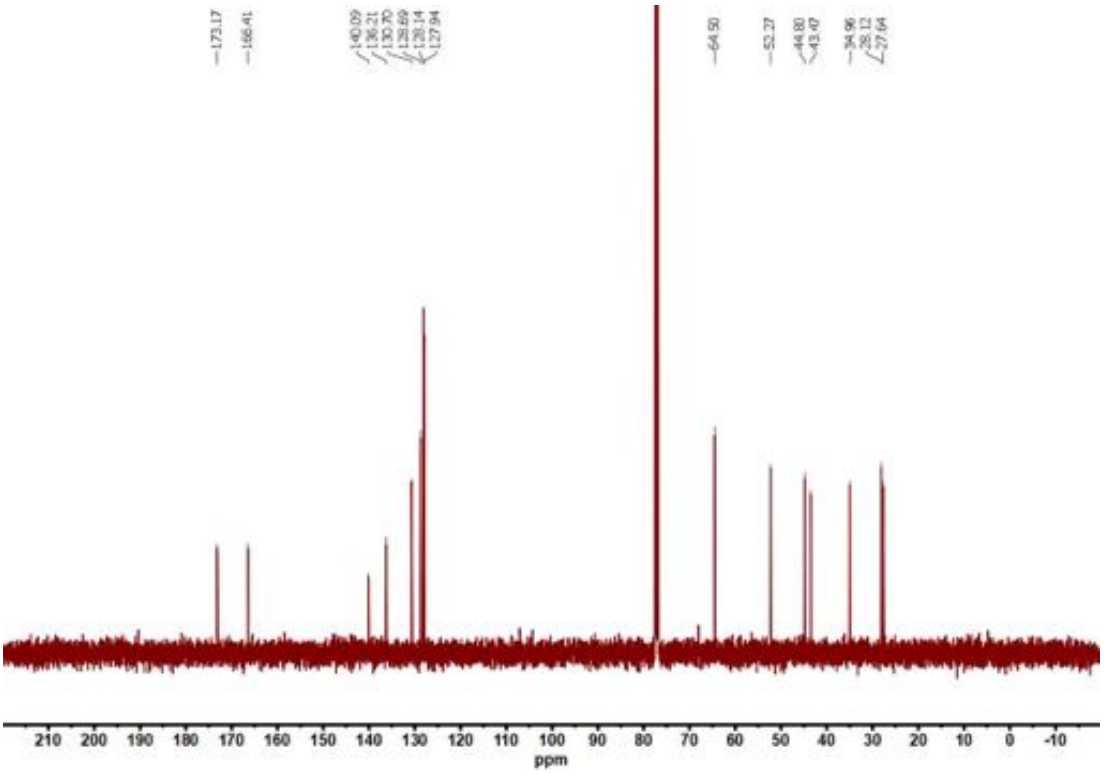

^{13}C NMR (126 MHz, $CDCl_3$) spectrum of **C1**

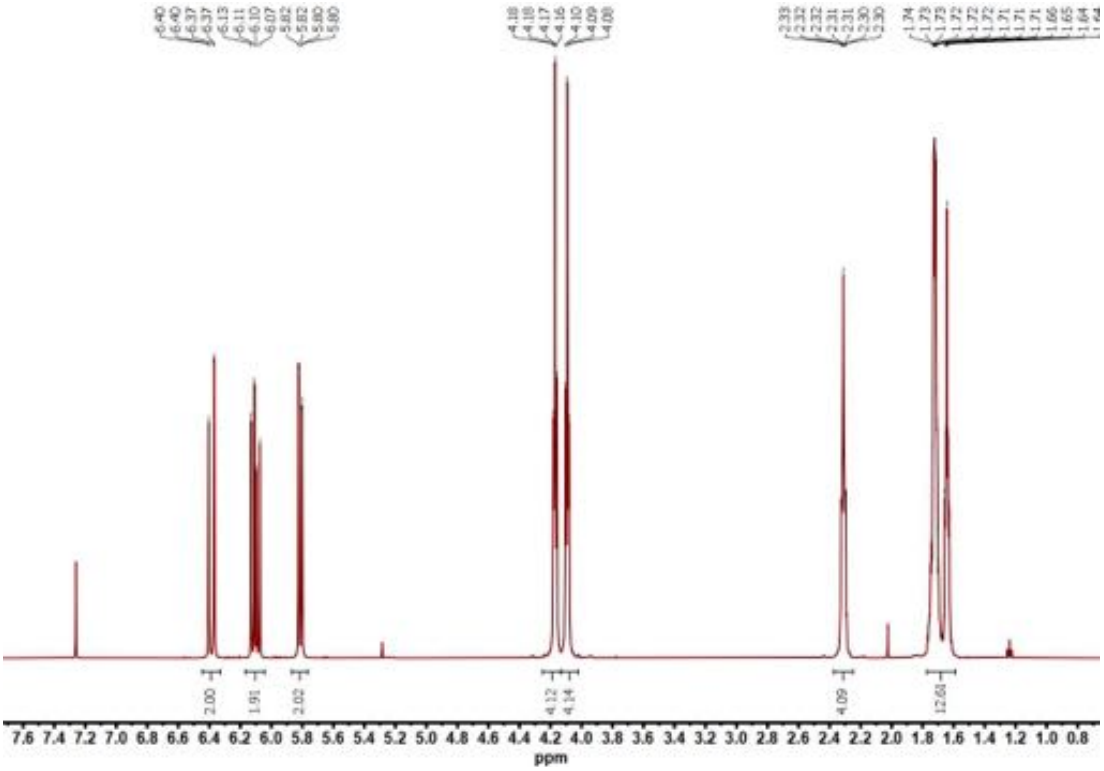

^{1}H NMR (500 MHz, $CDCl_3$) spectrum of **C2**

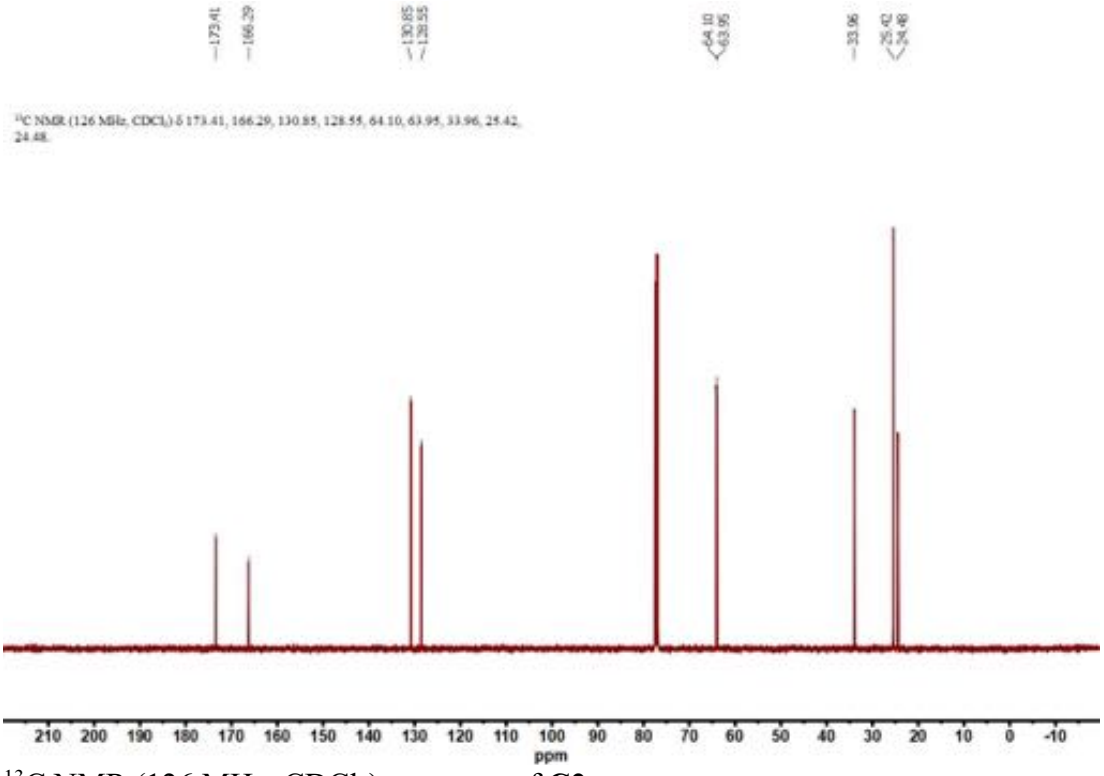

^{13}C NMR (126 MHz, $CDCl_3$) spectrum of **C2**

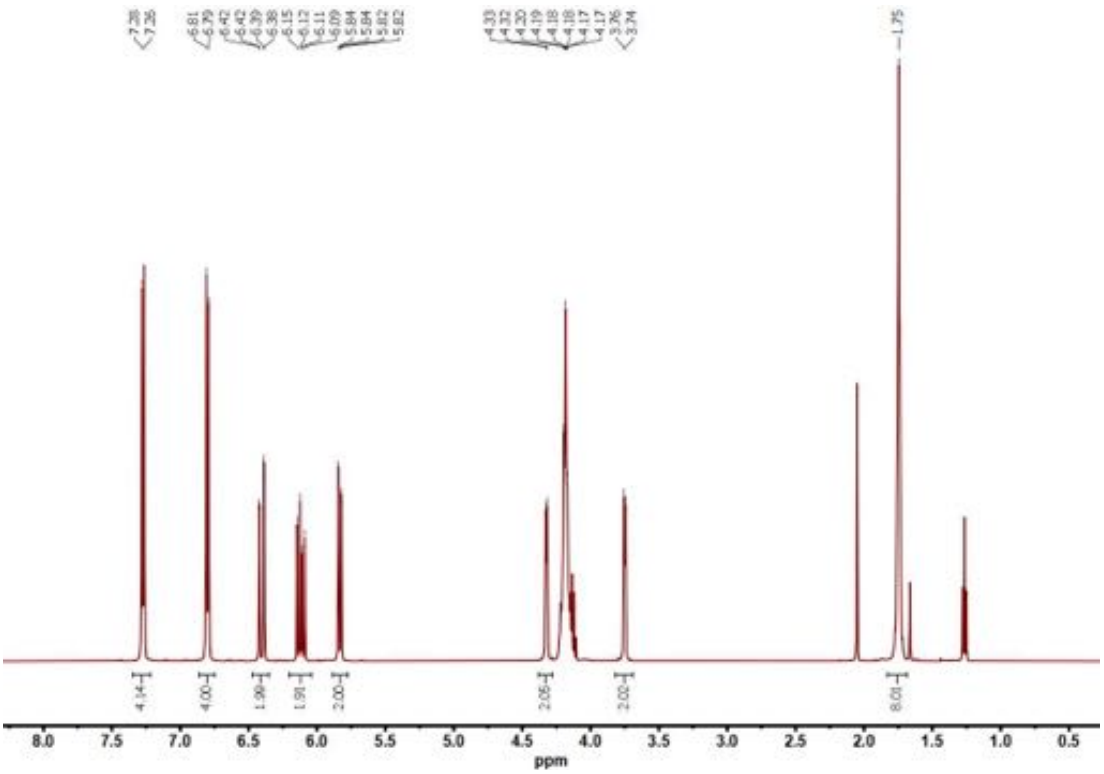

^{1}H NMR (500 MHz, $CDCl_3$) spectrum of **C3**

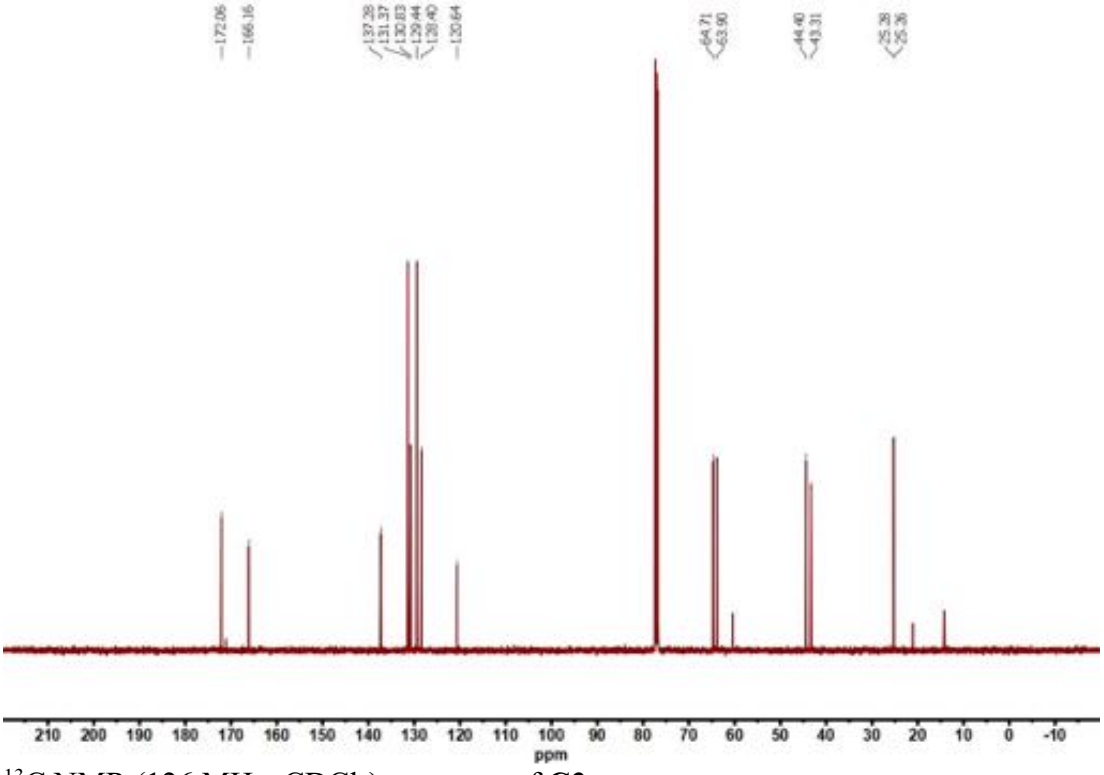

^{13}C NMR (126 MHz, $CDCl_3$) spectrum of **C3**

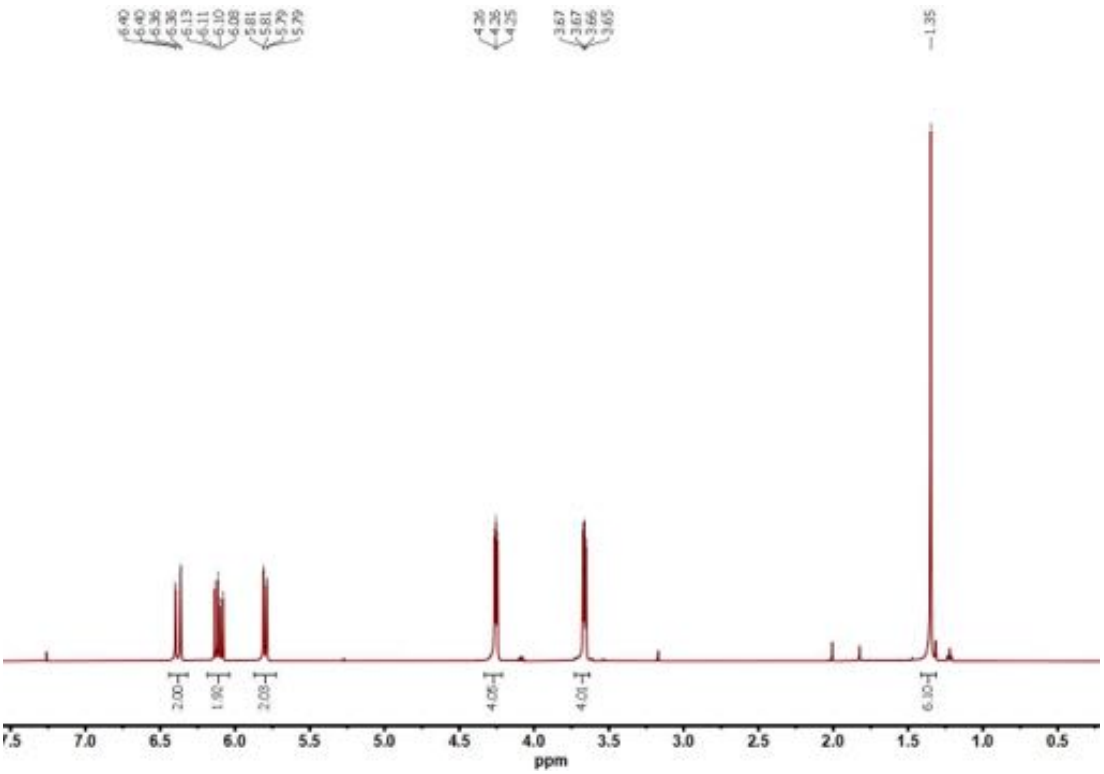

^{1}H NMR (500 MHz, $CDCl_3$) spectrum of **C4**

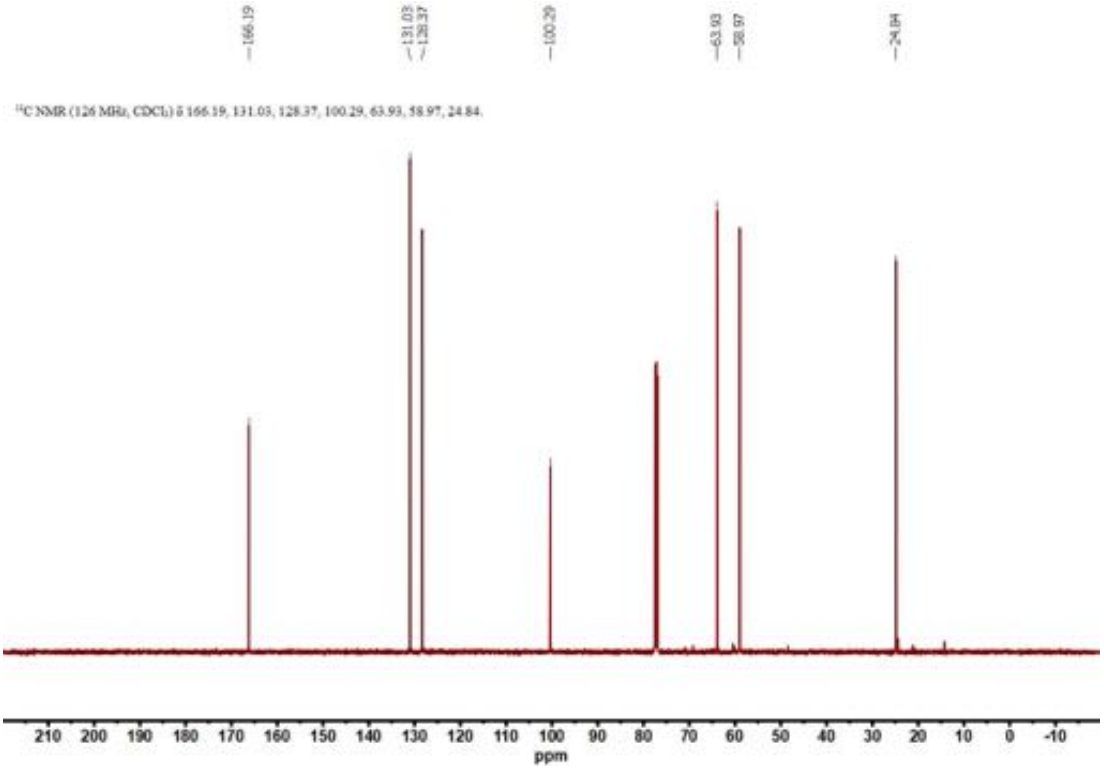

^{13}C NMR (126 MHz, $CDCl_3$) spectrum of **C4**

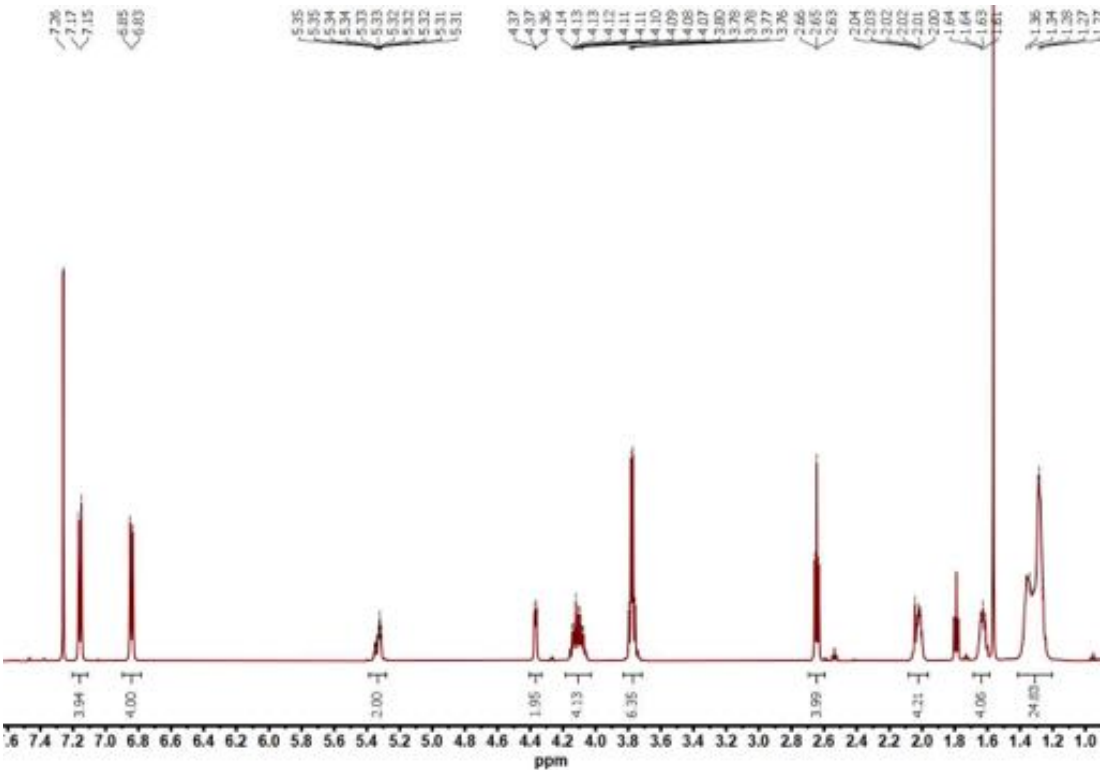

^{1}H NMR (500 MHz, $CDCl_3$) spectrum of **1g**

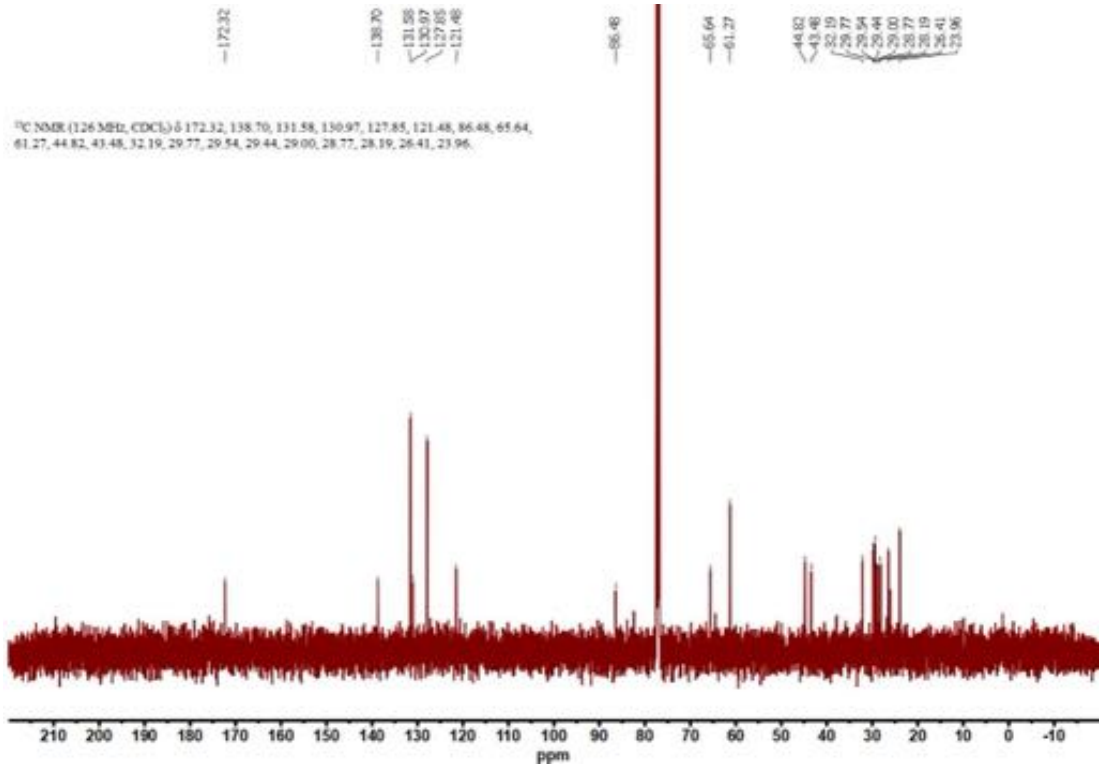

^{13}C NMR (126 MHz, $CDCl_3$) spectrum of **1g**

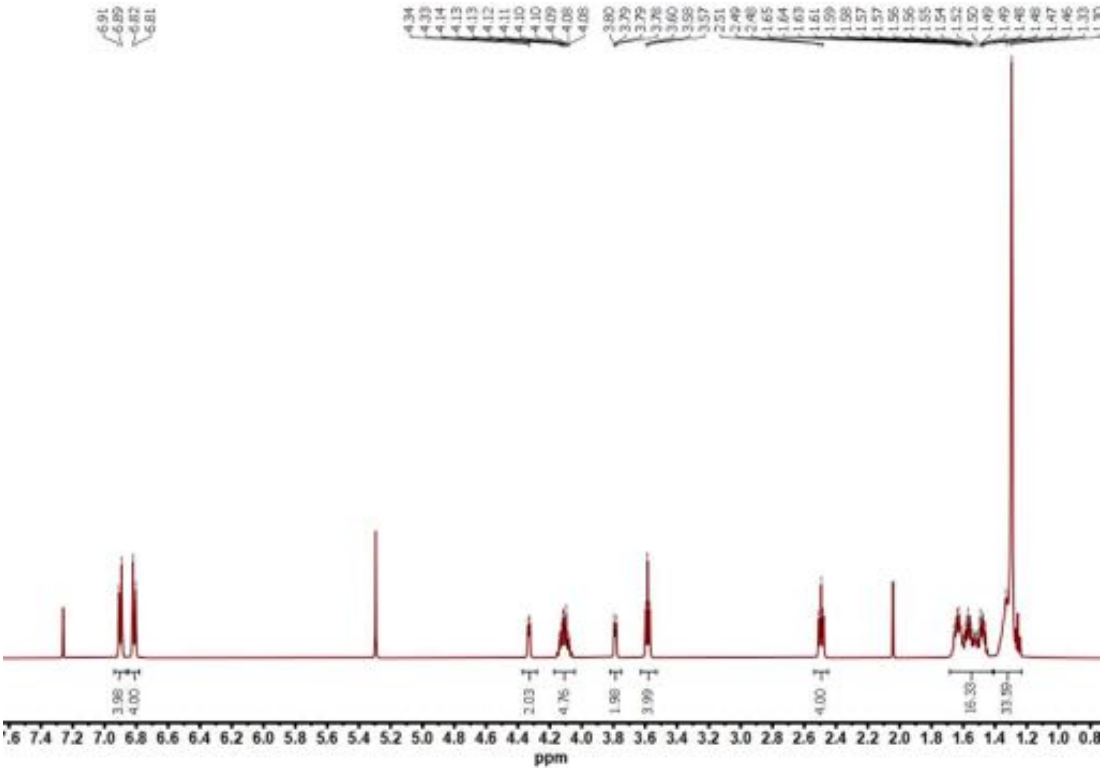

^{1}H NMR (500 MHz, $CDCl_3$) spectrum of **1h**

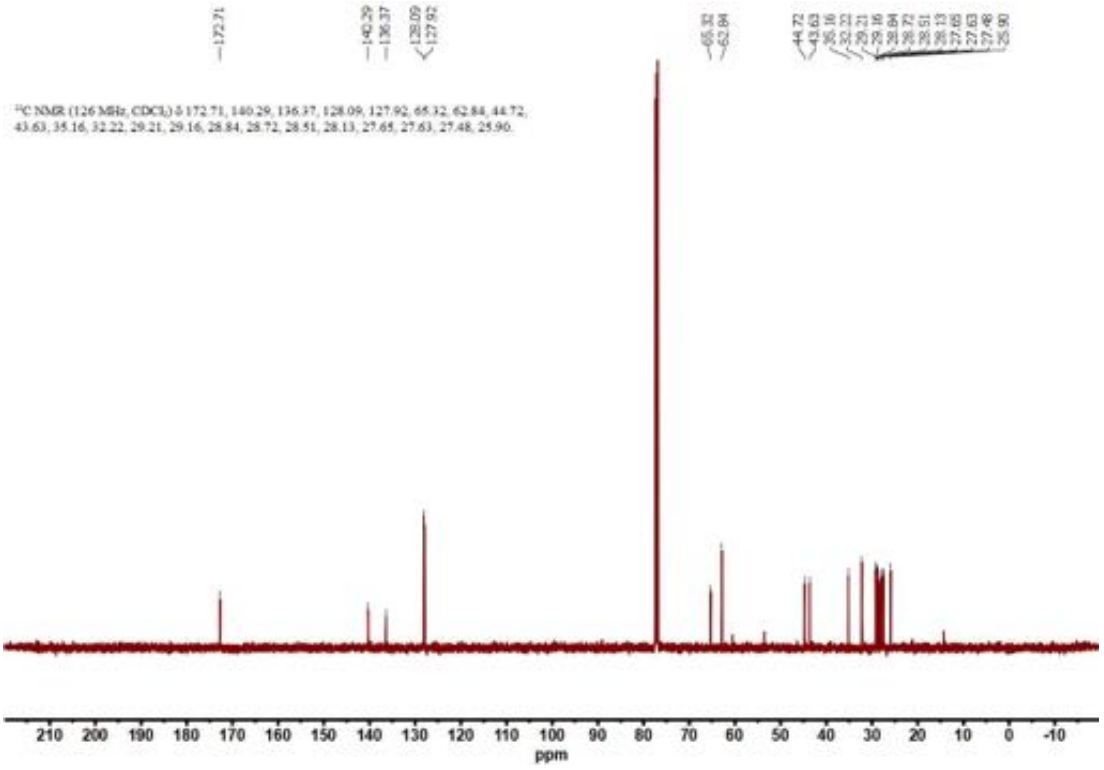

^{13}C NMR (126 MHz, $CDCl_3$) spectrum of **1h**

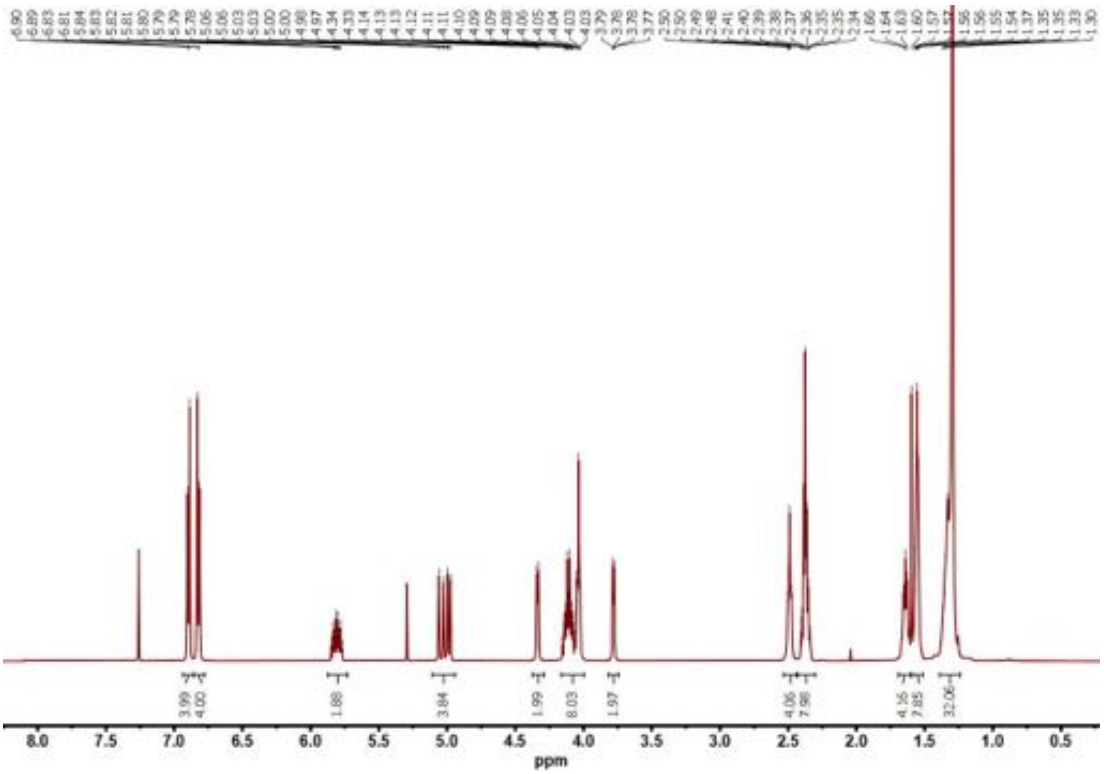

^{1}H NMR (500 MHz, $CDCl_3$) spectrum of **1i**

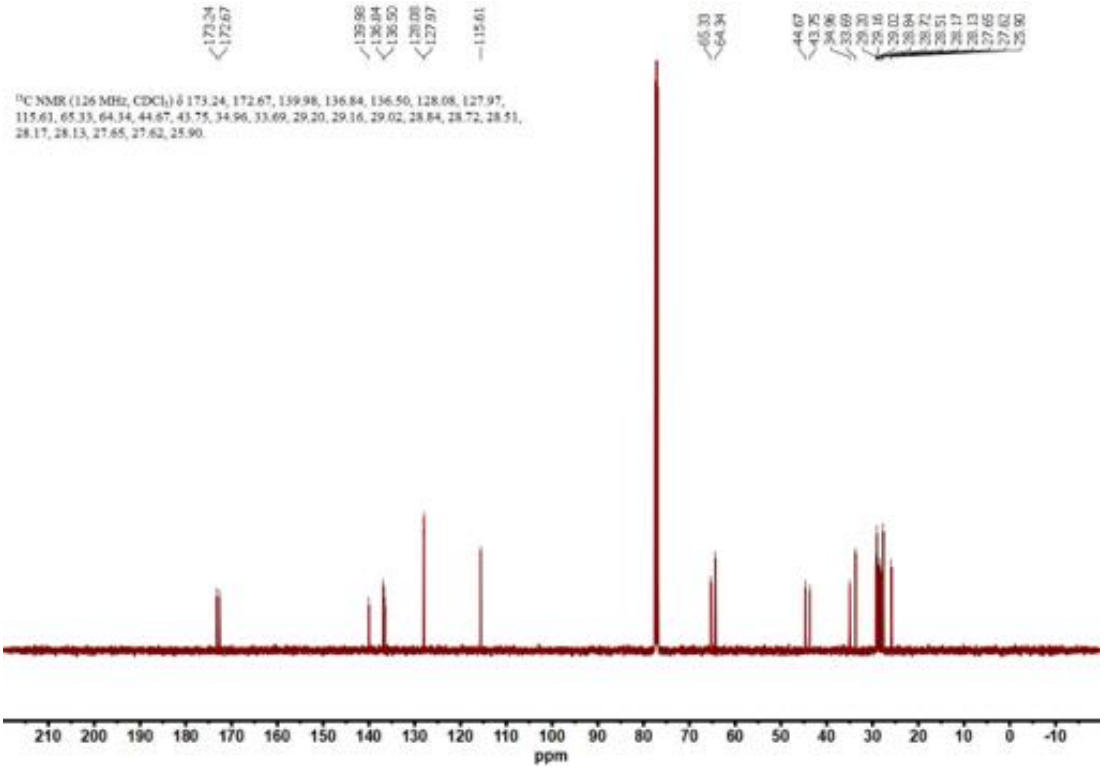

^{13}C NMR (126 MHz, $CDCl_3$) spectrum of **1i**

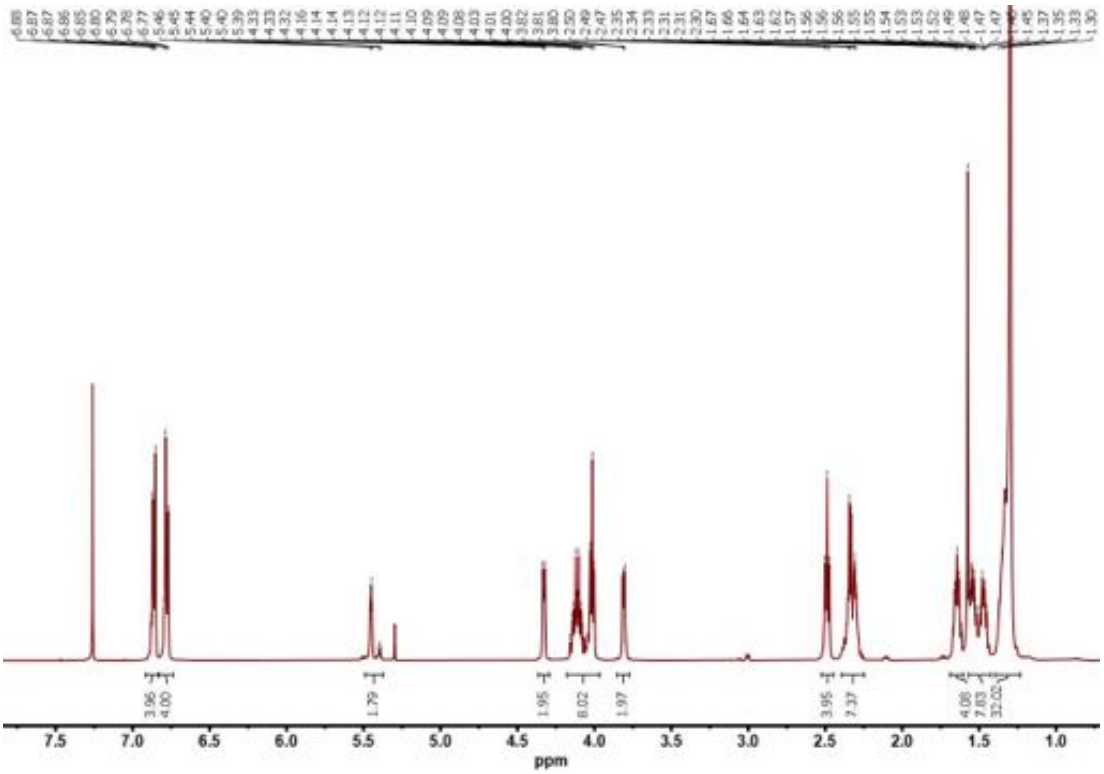

^{1}H NMR (500 MHz, $CDCl_3$) spectrum of **1j**

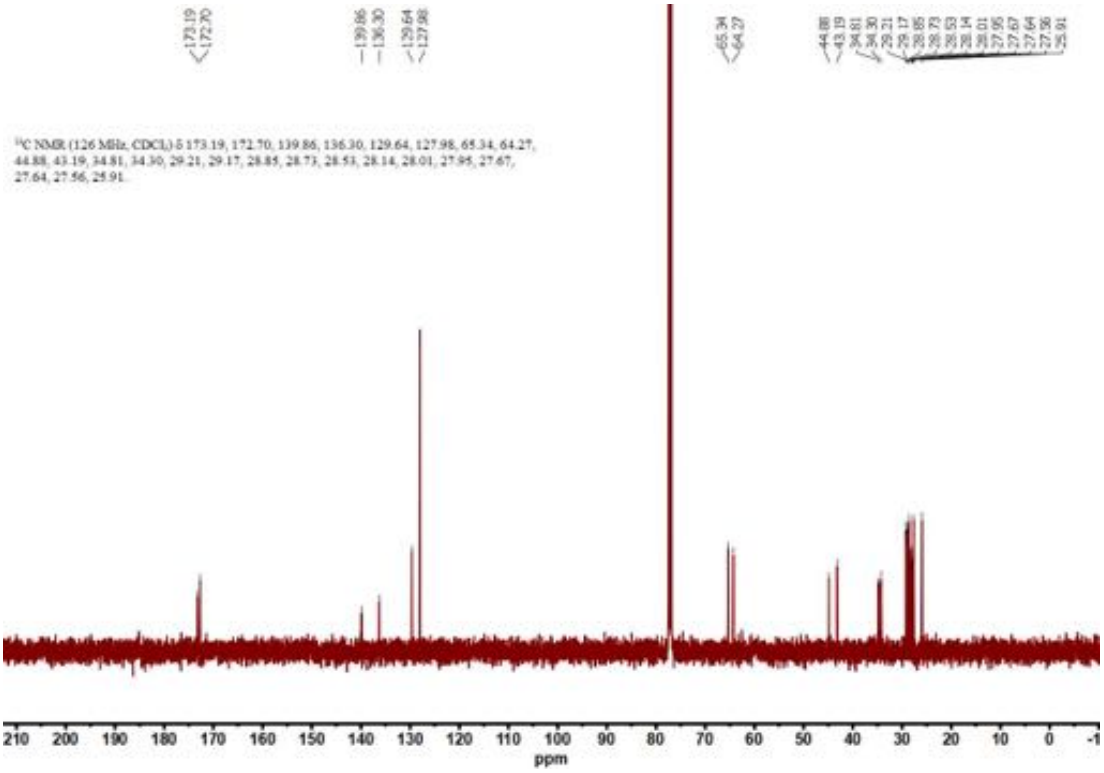

^{13}C NMR (126 MHz, $CDCl_3$) spectrum of **1j**

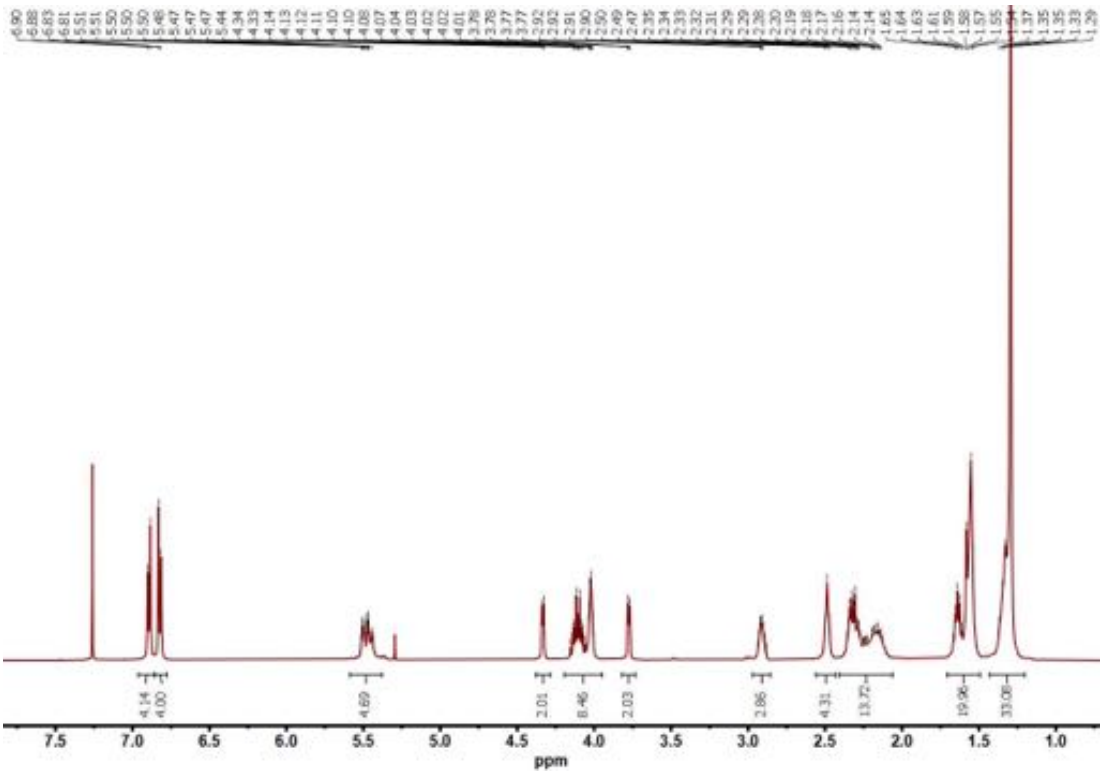

^{1}H NMR (500 MHz, $CDCl_3$) spectrum of **P1**

Movie S1. Comparison between notched samples of **E1** (left) and **E2** (right) under the same load condition. Elastomers were prepared with a stoichiometry of [M] : [C] : [CTA] : [PI] = 1 : 1/50 : 1/1200 : 1/2000. The video is 16× of real time.

References

24. Wu, D., Lenhardt, J. M., Black, A. L., Akhremitchev, B. B. & Craig, S. L. Molecular Stress Relief through a Force-Induced Irreversible Extension in Polymer Contour Length. *J. Am. Chem. Soc.* 132, 15936–15938 (2010).

25. Klukovich, H. M., Kouznetsova, T. B., Kean, Z. S., Lenhardt, J. M. & Craig, S. L. A backbone lever-arm effect enhances polymer mechanochemistry. *Nat. Chem.* 5, 110–114 (2013).

26. Wang, J., Kouznetsova, T. B., Niu, Z., Ong, M. T., Klukovich, H. M., Rheingold, A. L., Martinez, T. J. & Craig, S. L. Inducing and quantifying forbidden reactivity with single-molecule polymer mechanochemistry. *Nat. Chem.* 7, 323–327 (2015).

27. Wang, J., Kouznetsova, T. B., Niu, Z., Rheingold, A. L. & Craig, S. L. Accelerating a Mechanically Driven anti-Woodward-Hoffmann Ring Opening with a Polymer Lever Arm Effect. *J. Org. Chem.* 80, 11895–11898 (2015).

28. Kouznetsova, T. B., Wang, J. & Craig, S. L. Combined Constant-Force and Constant-Velocity Single-Molecule Force Spectroscopy of the Conrotatory Ring Opening Reaction of Benzocyclobutene. *Chemphyschem* 18, 1486–1489 (2017).

29. Oberhauser, A. F., Marszalek, P. E., Erickson, H. P. & Fernandez, J. M. The molecular elasticity of the extracellular matrix protein tenascin. *Nature* 393, 181–185 (1998).

30. Florin, E. L., Rief, M., Lehmann, H., Ludwig, M., Dornmair, C., Moy, V. T. & Gaub, H. E. Sensing specific molecular interactions with the atomic force microscope. *Biosens. Bioelectron.* 10, 895–901 (1995).

31. Chen, L., Sun, T. L., Cui, K., King, D. R., Kurokawa, T., Saruwatari, Y. & Gong, J. P. Facile synthesis of novel elastomers with tunable dynamics for toughness, self-healing and adhesion. *J. Mater. Chem. A* 7, 17334–17344 (2019).

32. Wang, J., Kouznetsova, T. B., Boulatov, R. & Craig, S. L. Mechanical gating of a mechanochemical reaction cascade. *Nat. Commun.* 7, 13433 (2016).

33. S. Plimpton, Fast parallel algorithms for short-range molecular dynamics. *J. Comput. Phys.* 117, 1–19 (1995).

34. G. S. Grest, K. Kremer, Molecular dynamics simulation for polymers in the presence of a heat bath. *Phys. Rev. A (Coll Park).* 33, 3628–3631 (1986).

35. K. Kremer, G. S. Grest, Dynamics of entangled linear polymer melts: A molecular-dynamics simulation. *J. Chem. Phys.* 92, 5057–5086 (1990).

36. J. K. Johnson, J. A. Zollweg, K. E. Gubbins, The Lennard-Jones equation of state revisited. *Mol. Phys.* 78, 591–618 (1993).

37. D. Frenkel, B. Smit, *Understanding molecular simulation: from algorithms to applications* (Academic Press, 2002).

38. J. D. Halverson, W. B. Lee, G. S. Grest, A. Y. Grosberg, K. Kremer, J. D. Halverson, W. B. Lee, G. S. Grest, A. Y. Grosberg, Molecular dynamics simulation study of nonconcatenated ring polymers in a melt . II . Dynamics. *J. Chem. Phys.* 134, 204905 (2011)

39. L. Leibler, F. Schosseler, Gelation of Polymer Solutions: An Experimental Verification of the Scaling Behavior of the Size Distribution Function. *Phys Rev Lett.* 55, 1110–1113 (1985).

40. G. S. Grest, K. Kremer, Statistical Properties of Random Cross-Linked Rubbers. *Macromolecules.* 23, 4994–5000 (1990).

41. P. G. de Gennes, On a relation between percolation theory and the elasticity of gels. *Journal de Physique Lettres.* 37, 1–2 (1976).

42. Proceedings of the Python in Science Conference (SciPy): Exploring Network Structure, Dynamics, and Function using NetworkX, (available at https://conference.scipy.org/proceedings/SciPy2008/paper_2/).

43. K. Paton, An algorithm for finding a fundamental set of cycles of a graph. *Commun. ACM.* 12, 514–518 (1969).

44. P. M. Morse, Diatomic molecules according to the wave mechanics. II. Vibrational levels. *Phys. Rev.* 34, 57–64 (1929).